ARL-MR-1161 • Sep 2026

DEVCOM ARMY RESEARCH LABORATORY

AMD-CFT (CG4) Photonic Integrated Circuit Time-Delay Beamformer

Stephen R. Anderson

DISTRIBUTION STATEMENT A. Approved for public release; distribution is unlimited.

NOTICES

Disclaimers

The findings in this report are not to be construed as an official Department of the Army position unless so designated by other authorized documents.

Citation of manufacturer's or trade names does not constitute an official endorsement or approval of the use thereof.

Destroy this report when it is no longer needed. Do not return it to the originator.

ARL-MR-1161 ● Sep 2026





AMD-CFT (CG4) Photonic Integrated Circuit Time-Delay Beamformer

Stephen R. Anderson
DEVCOM Army Research Laboratory

DISTRIBUTION STATEMENT A. Approved for public release; distribution is unlimited.

REPORT DOCUMENTATION PAGE

1. REPORT DATE	2. REPORT TYPE	3. DATES COVERED	
		START DATE	END DATE
SEPTEMBER 2026	MEMORANDUM REPORT	OCT 2020	SEP 2026

4. TITLE AND SUBTITLE

AMD-CFT (CG4) Photonic Integrated Circuit Time-Delay Beamformer

5a. CONTRACT NUMBER	5b. GRANT NUMBER	5c. PROGRAM ELEMENT NUMBER
5d. PROJECT NUMBER	**5e. TASK NUMBER**	**5f. WORK UNIT NUMBER**

6. AUTHOR(S)
Stephen R. Anderson

7. PERFORMING ORGANIZATION NAME(S) AND ADDRESS(ES)
DEVCOM Army Research Laboratory
ATTN: FCDD-RLA-PC
ADELPHI, MD 20783

8. PERFORMING ORGANIZATION REPORT NUMBER
ARL-MR-1161

9. SPONSORING/MONITORING AGENCY NAME(S) AND ADDRESS(ES)	10. SPONSOR/MONITOR'S ACRONYM(S)	11. SPONSOR/MONITOR'S REPORT NUMBER(S)

12. DISTRIBUTION/AVAILABILITY STATEMENT
DISTRIBUTION STATEMENT A. Approved for public release; distribution is unlimited.

13. SUPPLEMENTARY NOTES
ORCID: Stephen R. Anderson, 0000-0001-9211-5646

14. ABSTRACT
Photonic integrated circuits (PICs) provide a low size, weight, power, and cost platform for high-speed analog signal processing. Radio frequency beamforming of phased array antennas benefit from fine control of broadband signal delay, which is achieved through photonic integrated circuit true-time delay architectures. PICs were designed, modeled, and then fabricated in the AIM Photonics foundry. Generating true-time-delay with a three-bit ring-mediated switching architecture and a continuously tunable Mach-Zehnder-interferometer-mediated architecture is explored. Practical challenges of resonant-device uniformity and thermo-optic control are identified. This report summarizes measured data collected on photonic circuit true-time delay beamforming to support Army Air and Missile Defense priorities.

15. SUBJECT TERMS
Air and Missile Defense, Photonic Integrated Circuit, Phased Array Antenna, Time Delay, Silicon Photonics, Electronic Interposer

16. SECURITY CLASSIFICATION OF:			17. LIMITATION OF ABSTRACT	18. NUMBER OF PAGES
a. REPORT	b. ABSTRACT	C. THIS PAGE		
UNCLASSIFIED	UNCLASSIFIED	UNCLASSIFIED	SAR	61

19a. NAME OF RESPONSIBLE PERSON	19b. PHONE NUMBER *(Include area code)*
Stephen R. Anderson	(+1) 520-691-5408

STANDARD FORM 298 (REV. 5/2020)
Prescribed by ANSI Std. Z39.18

Contents

List of Figures v

List of Tables ix

Acknowledgments x

Executive Summary xi

1. Introduction 1

2. True Time Delay 1

3. Time Delay Architectures 2

3.1 Switched Delays 4

3.2 Switch with Feedback 8

3.3 Wavelength Division Multiplexed Delays 11

4. Device Fabrication 12

5. Resonator-Switched Delay Circuit 17

5.1 Variable Ratio Power Tap Design 21

5.2 Ring Resonator Characterization 24

5.3 Catastrophic Optical Damage in AIM Platform 26

5.4 Tuned Ring Resonator TTD Unit 27

6. MZI-Switched Delay Circuit with Interposer 30

6.1 Device Characterization 33

6.2 Wideband Phased Array Antenna 37

7. Conclusions 39

8. References 41

Appendix. Derivation of Group Delay **42**

List of Symbols, Abbreviations, and Acronyms **45**

Distribution List **47**

List of Figures

Figure 1. The transmission magnitude, phase, and group delay of an ideal TTD system. For example, traveling through an increasingly longer length of a dispersion-less channel induces a perfect tunable TTD. ……3

Figure 2. a) Conceptual path-length switching using two DPDT switches with cross-over wiring. b) Circuit diagram of a path-length controlled optical delay line utilizing two TOSs. ……5

Figure 3. The transmission magnitude, phase, and group delay through the TOS delay line about the base-band center frequency. ……7

Figure 4. The transmission magnitude, phase, and group delay through the TOS delay line about the base-band center frequency. A feedback waveguide connects the auxiliary output $\overline{Out}$ with the upper-right input port. These simulated results represent an ideal case where waveguide attenuation is $0\,\mathrm{dB\,cm^{-1}}$. ……9

Figure 5. The transmission magnitude, phase, and group delay through the TOS delay line about the base-band center frequency. A feedback waveguide connects the auxiliary output $\overline{Out}$ with the upper-right input port. A constant waveguide attenuation of $2\,\mathrm{dB\,cm^{-1}}$ is assumed. …… 10

Figure 6. The transmission magnitude, phase, and group delay through the TOS delay line about the base-band center frequency. A feedback waveguide connects the auxiliary output $\overline{Out}$ with the upper-right input port. A constant waveguide attenuation of $2\,\mathrm{dB\,cm^{-1}}$ is assumed. Detail sweep to show the null transmission condition. …… 11

Figure 7. A cascade of ring resonators. For each choice of λ, the signal travels an increasingly longer path, adding an additional 2Δ L path length for each wavelength channel i from 1 to N. …… 12

Figure 8. AIM Photonics Full Active Layer Stack.[5] …… 13

Figure 9. AIM Photonics Electronic Interposer Layer Stack.[6] …… 14

Figure 10. a) The layout of MPW run 22-02A, with blue-highlighted region containing 30 TTD units each made from a cascade of 10 WDM-separated ring resonators. b) Detail view of the power tap PDK cell, which comes in two power-splitting variations: 1% and 10% power-splitting ratios. c) Detail view of one WDM ring-resonator cell.…… 15

Figure 11. Measured transmission through a 10 ring x 30 stage beamformer.… 16

Figure 12. Spectral shift of 10-ring cascade as a function of substrate temperature. 17

Figure 13. System block diagram with TTD cell exploded view. The signal enters at the IN port and accumulates a binary multiple of a design delay ΔL in the TTD component. A small fraction of the signal taps through an optical splitter (denoted "%") into a beamformer output. The majority of the signal transmits into the next TTD unit, accumulating additional TTD. 18

Figure 14. The fabricated layout of a 30-element beamformer on the 24-01A full-active MPW chip. Other MPW projects on the die are omitted. One TTD cell, composed of three independently tuned ring resonator switches, is depicted in the TTD Unit Detail view. A micrograph of the corresponding fabricated chip TTD unit is also shown, with one ring resonator "RR" and splitter "%" highlighted. 19

Figure 15. Interposer-less direct-mounting of PIC [24-01A] on PCB. 20

Figure 16. Wirebonded test assembly of a PIC connected to Nicslab multi-channel SMU and fiber array. 20

Figure 17. Target output coupling constants K for an N=30 element beamformer to achieve uniform output power. 22

Figure 18. Physical layout of a parameterized splitting-ratio directional coupler. The inter-waveguide coupling gap and the coupling length vary to obtain the desired power tap ratio. 22

Figure 19. Curve-fits of coupling constant versus coupling length for various as-fabricated gap widths at 1550 nm. 23

Figure 20. Final splitting-ratio to coupling-length lookup table for selected coupling gap widths of 200, 300, and 400 nm. 24

Figure 21. Ring heater I-V curves referenced to the PDK reported 200 Ω nominal resistance. 24

Figure 22. Excess current in ring resonator's heater due to applied optical power. 26

Figure 23. Catastrophic device failure. Blackened material formed on the first input ring resonator on this silicon die. (Top Left) Standard AIM Photonic PDK ring resonator. (Top Right) Ring resonator after damage. (Bottom) SWIR image of light ejecting out of the damaged ring. 27

Figure 24. Linear transfer function measurement using a Luna optical vector analyzer. 28

Figure 25. Measured transverse-electric polarized transmission and phase response of one 3-bit tuned-resonator TTD element. A small graphic on the right depicts where the applied voltage is being swept for each transmission and phase plot. 29

Figure 26. Schematic diagram for time-delay oscilloscope capture. 30

Figure 27. Side view of the planned PIC + interposer + PCB stack. 31

Figure 28. Chip 24-02A schematic and fabricated layout. Left: The 10-element MZI-type TTD serial beamformer circuit is shown in schematic view. Right: A detail view of arrayed bond pads intended for flip-chip bonding to the 24-04E interposer, above a few of the TOSs and spiral delay lines that form the TTD elements. 32

Figure 29. Schematic view (X-ray) of AIM chip 24-02A (red outline) flip-chip attached to the interposer 24-04E. 33

Figure 30. On-chip AIM PDK analog photodetector response versus reverse bias voltage as a function of input power. 34

Figure 31. Transmission through one TTD MZI as a function of input and output TOS heater current: (left) simulated response; (right) measured response with axes rescaled to provide a direct comparsion. 35

Figure 32. Output photocurrent as a function of MZI heater sweep. Each curve represents a different switching state configured by the input and output TOS heater settings (H1 and H2) co-varying. 36

Figure 33. Output photocurrent as a function of the input TOS heater current at select output TOS heater current switch states. The MZI heater is undriven. 36

Figure 34. RF simulations of transmission line impedance versus trace width on the fan-out PCB. 37

Figure 35. (Left) 30-element 10-GHz Vivaldi-type antenna array with coaxial feeds. Fabricated at C5ISR's PIF (March 2026). (Right) Simulated beam for only 10 driven elements at selected steering angles. 38

Figure 36. C5ISR PIF fabricated antenna with RF cable feedlines. 38

Figure 37. Azimuthal gain profile for the centered (Port 15) emitter. Vertically polarized. 39

Figure A-1. Jax gradient computation of group delay provides instantaneous computation of group delay at a chosen frequency. The finite difference method can also obtain the group delay accurately but suffers at small offset frequencies due to numerical error. 44

List of Tables

Table 1. AIM run identification. 13

Acknowledgments

I'd like to thank Dr. Audrey Rose Gutierrez (ORAU) for her help wirebonding samples and Drs. Weimin Zhou and Justin Bickford (ARL) for their mentorship.

Executive Summary

Photonic integrated circuits (PICs) offer a low size, weight, power, and cost (SWAP-C) pathway for analog signal processing. Signals modulated into the optical domain can be processed with bandwidths that exceed the capabilities of pure radio-frequency circuits. This report documents design and measurement of signal manipulation on a domestically sourced PIC platform to facilitate on-chip true time delays for steering an RF beam from a wideband phased array antenna (PAA). This line of effort intended to explore the creation of an RF-photonic process stack featuring a photonic integrated circuit flip-chip attached to an electronic interposer. This effort faced a major setback in the fabrication cycle at the AIM Photonics foundry. The run schedule for a full-active process takes 5 months, and the published run schedule for an electronic interposer is 3 months. The electronic interposer we ordered took 17 months to arrive, which has pushed full integration of the photonic stack to an antenna outside the scope of this report. We expect to complete this work in the future. Densely integrated photonic circuits with interposer fan-out remain an enabling technology for RF photonic applications, and our exercise of the AIM foundry has successfully resulted in new process development within the foundry to solve the production problems that led to this delay.

PICs were designed and fabricated to explore various methods of generating true time delay through circuit architectures that implement wavelength division multiplexed and switched-path delays. Two approaches that utilize switched-paths were considered. One implementation characterized digital beamforming using a 3-bit ring-mediated switching architecture. This was intended to steer a wideband analog waveform to predetermined directions. Measurement and analysis of this device provided a clearer picture of how it operates and how it might be repurposed as a reconfigurable filter. It also served as a testbed to improve our PIC assembly, packaging, and experimental test techniques. The second switched-path approach characterized a continuously tunable delay using a Mach-Zehnder-interferometer-mediated architecture. This circuit was intended for use in the interposer demonstrator. Experimental characterization of these circuits revealed practical information, established optical power limits, and demonstrated the use of laboratory equipment for controlling the PIC configuration.

This knowledge will be useful in future efforts to save circuits from damage and to increase our body of knowledge of photonic simulation and measurement techniques.

A collaboration with the U.S. Army Combat Capabilities Development Command (DEVCOM) C5ISR also resulted in the design and fabrication of a companion phased array antenna that can serve as the testbed for wideband, agile, photonic-controlled RF beamforming, and may lead to transition opportunities. This work also leveraged funding from the tri-service Microelectronic Commons project EPIC-BEAMS.

1. Introduction

The phased array antenna (PAA) is an antenna architecture for manipulating the far-field beam aperture and steering direction by using many (potentially thousands) spatially distributed emitters. These emitters may be relatively simple on their own, such as a patch antenna that radiates isotropically, but when combined in a phased array, they can produce a beam with a defined waist and steering direction. Antenna design, including the emitters and their particular spatial arrangement, is outside the scope of this report. In order for a phased array to operate, the signal at each emitter must be carefully controlled in amplitude and phase. In this report, we will detail efforts to impart true time delay (TTD) onto a wideband signal using analog signal processing on a photonic integrated circuit (PIC).

2. True Time Delay

First, we briefly review and define terms for processing analog signals. For any linear time-invariant (LTI) signal processing system, the complex-valued transfer function H can be decomposed into an amplitude and phase response with respect to frequency f.

$$H(\omega) = |H(\omega)|\, e^{j\phi(\omega)} \tag{1}$$

where $\omega = 2\pi f$. Imparting a time delay τ to a signal induces a phase shift proportional to that time delay: $\Delta\phi(\omega) = -\omega\tau = -2\pi f\tau$. We adopt the convention that a positive time delay induces a negative phase shift. At an instantaneous frequency f_0, a phase-shifted sinusoidal signal exiting an LTI system can be equivalently regarded as having experienced a time delay $\Delta\tau_{phase}$. This time delay may be referred to as a phase delay.

$$\Delta\tau_{phase} = -\phi(\omega)/\omega \tag{2}$$

The carrier wave propagating through a medium experiences a phase delay. In contrast, the signal information modulated onto that carrier moves with an apparent velocity. The time delay of this signal envelope is given by the group delay:

$$\Delta\tau_{group} = -\frac{\delta\phi(\omega)}{\delta\omega} \tag{3}$$

When a signal has transited an LTI system under a pure time shift, the system is considered to have experienced a TTD. For all frequency components in the signal, which may be wideband, the time shift is equal. For this condition to hold, the group delay within the signal bandwidth must be constant $\tau_{group} = \tau_0$. This occurs when the phase response of the system is linearly proportional to frequency:

$$\phi(\omega) = -\tau_0\omega + \phi_0 \tag{4}$$

3. Time Delay Architectures

We assess the design of various photonic waveguiding devices to create tunable TTD. We consider their theory of operation. Later, measurements of actual devices using these architectures will be discussed.

The phase response of a standard integrated photonic waveguide is described by its propagation constant $\beta = 2\pi n_{eff}\lambda^{-1}$, where n_{eff} is the effective index of the propagating mode. Accordingly, the phase change imparted through a length ΔL of waveguide accumulates phase $\Delta\phi = \beta\Delta L$, and causes a change in the group delay:

$$\Delta\tau_{group} = -\frac{n_{eff}\Delta L}{c} \tag{5}$$

if and only if n_{eff} is dispersion-less. Else, as $n_{eff} \rightarrow n_{eff}(\omega)$:

$$\begin{aligned}\Delta\tau_{group} &= -\frac{\Delta L}{c}[\frac{\delta}{\delta\omega}\omega n_{eff}(\omega)] \\ &= -\frac{\Delta L}{c}[n_{eff}(\omega) + \omega\frac{\delta n_{eff}(\omega)}{\delta\omega}] \\ &= -\frac{\Delta L}{c}n_{group}\end{aligned} \tag{6}$$

The group delay can be adjusted by modifying various physical parameters of the channel transited by the signal, either the effective index n_{eff} or the path length L.

The effective index depends on the physical dimensions of the waveguide as well as the material index of each of its constituent core and cladding materials. Changes in either structure or material properties—due to mechanical strain, temperature, or the

injection of free carriers—allow for control over the channel effective index over a range of timescales and magnitudes. Wavelength-division multiplexed systems can exploit the inherent wavelength dependence of the effective index, changing the carrier wavelength to impart a change in the group delay. Other mechanisms for changing phase can leverage nonlinear effects such as intensity-dependent or magneto-optical index changes. Our ideal transfer function is depicted in Figure 1, where the channel imparts lossless transmission, linear phase, and increasing, constant, and broadband time delay as a function of a provided control signal. Likewise, mechanical-switch systems effect a group delay change by diverting the signal through an increased path length.

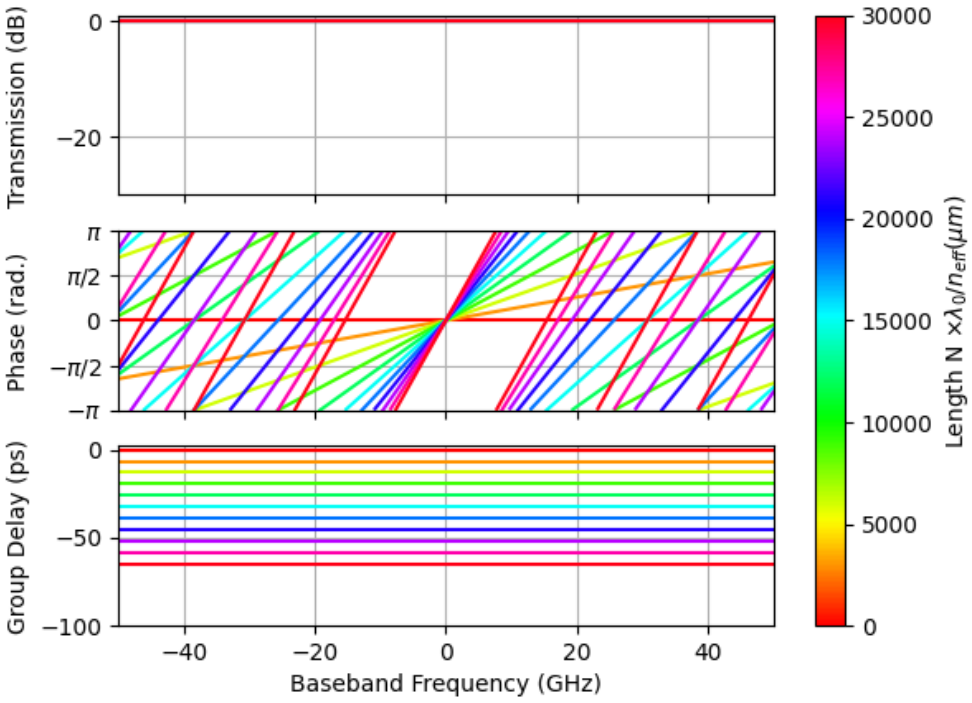


Figure 1. The transmission magnitude, phase, and group delay of an ideal TTD system. For example, traveling through an increasingly longer length of a dispersion-less channel induces a perfect tunable TTD.

There is significant research interest in the field of generating TTDs, and many architectures have been developed to generate optical true time delays (OTTDs) in the literature.[1] These have been identified, for example, as resonant or slow-light

based dispersive, multi-path switchable, and wavelength-selective OTTD. We will focus on the design, fabrication, and test of such devices in our domestic foundries. First, we will examine path length switched delays in Section 3.1. Then, we will discuss wavelength-division multiplexed approaches to delay in Section 3.3.

3.1 Switched Delays

In our integrated photonics platform, light confined in a waveguide can be diverted into another path using a thermo-optic switch (TOS) component, which has no moving parts. One implementation of a TOS is a matched-path Mach-Zehnder interferometer with a phase shifter in one or each arm. A 2×2 directional coupler splits light into each of the two matched paths. The phase shifter can impart a relative phase change into one of the paths, and light from both arms recombines in a second 2×2 directional coupler. The phase change can be chosen so that light constructively interferes into one output channel, while destructively interfering in the other output channel. Figure 2a presents an analogy to electrical circuitry, where the TOS has the characteristics of a four-way, double-pole, double-throw (DPDT) switch with a crossover switching state. A diagram of an OTTD line that switches between two waveguides with a path-length difference ΔL between them is depicted in Figure 2. A device with an equivalent netlist has been fabricated and assessed in recent literature in an indium phosphide material system,[2] producing upwards of 125 ps of tunable TTD. However, the internal structure of the TOS in this paper was an multi-mode interferometer (MMI) type, which does have a distinct transfer function compared to the directional couplers considered in this report. The following discussion will refer to devices possessing this netlist as a "Melati-type" delay line. A conceptual DPDT system can only access two distinct delay states: when the input and output switch are actuated, and when they are not. In contrast, TOSs are beneficial because the input and output switch can each access intermediate states where a fraction of optical power routes into each delay path. The resultant recombined signal at the output has a TTD that varies continuously with the smooth change in the switch power-splitting fraction. However, we will show that this smooth variation of time delay is band-limited.

Next, we will analyze the behavior of this Melati-type delay line under ideal conditions

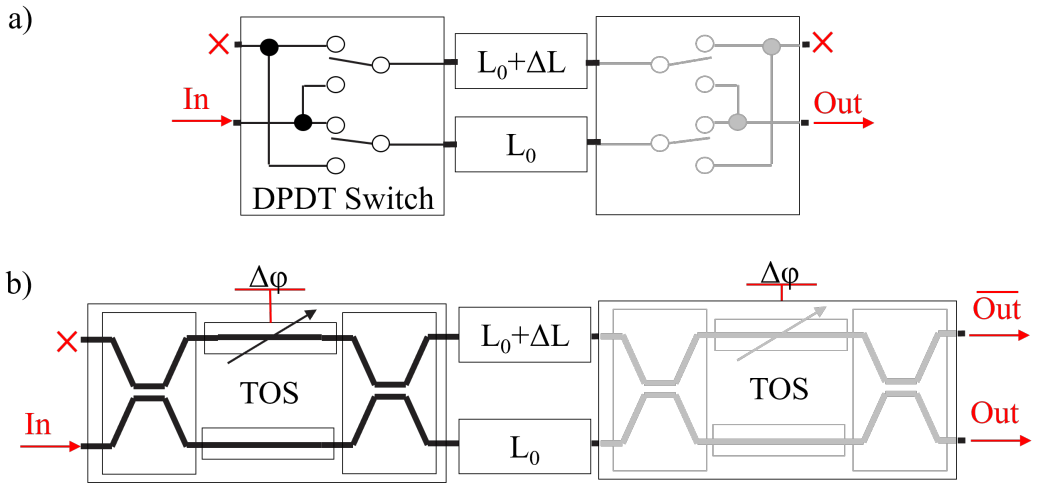


Figure 2. a) Conceptual path-length switching using two DPDT switches with cross-over wiring. b) Circuit diagram of a path-length controlled optical delay line utilizing two TOSs.

using the SAX (S + Autograd + XLA) package for Python, which is an S-parameter frequency-domain circuit simulation package built on JAX, a high-performance numerical computing package. We can use this package to compute the optical transfer function versus wavelength for any passive optical circuit. Or, we can consider how RF signals modulated about a central carrier wavelength are affected under different modulation formats by expressing the transfer function in a complex base-band representation about the provided central wavelength. To begin, we consider behavior when all waveguides have no dispersion ($n_{group} = n_{eff}$) and no attenuation per unit length. All fundamental 2×2 couplers are ideal, providing reciprocal, instantaneous, and loss-less power splitting between each input port and its two outputs, which implies a 90° phase shift applied to the cross port. Each TOS is formed from two ideal couplers, with a phase shifter in each arm.

In the limit where the coupling coefficient of the rightmost coupler in each TOS goes to zero (so that no light couples into the cross arm of the coupler), the configuration of Figure 2 reduces to a Mach-Zehnder interferometer with path length difference ΔL. The free spectral range (FSR) of the interferometer is given by

$$FSR[Hz] = \Delta\nu = \frac{c}{n_{group}\Delta L} = \Delta\tau_{group}^{-1} \tag{7}$$

where we can identify that the FSR is simply the inverse of the group delay difference between the two interferometer arm path lengths. The maximum transmission peak occurs when the phase difference between the two path lengths adds constructively, such that ΔL is an integer multiple of the effective wavelength of interest (λ_0/n_{eff}). Consider the construction $\Delta L = N \times (\lambda_0/n_{eff})$, $N \in \mathbb{Z}$. By specifying path lengths within our model using the multiplier N relative to the scaled wavelength, we can more directly construct path length differences that are intentionally in phase ($\Delta N \in \mathbb{Z}$) or out of phase ($\Delta N \in \mathbb{Z} + \frac{1}{2}$).

When centered on a maximum transmission peak in the MZI transfer function, the full-width, half maximum (FWHM) bandwidth spans one-half of the FSR. $FWHM = FSR/2$. Since the quantities of FSR and delay are inversely proportional, the bandwidth-delay product $FWHM \times \tau_{group}$ is constant.

With the behavior of the MZI in mind, we can consider the state of the Melati-type system when all couplers within the TOSs have equal (50%) power-splitting ratio. Under these conditions, adjusting the phase in one arm of the TOS allows the output to switch completely from one output to the other. The transfer function of the TOS-path delay line is depicted in Figure 3. Assigning port numbers counterclockwise from the lower-left port, the transfer function depicts the transmission magnitude $|S41|^2$ and the phase response $\angle(S41)$, along with the computed group delay, as a function of base-band frequency about the center carrier $\lambda_0 = 1.55\,\mu\text{m}$. The group delay is calculated directly from the sensitivity of the S-parameter matrix of the total system model, as discussed in the Appendix.

The phase shifter state of the two TOSs is varied simultaneously from $\phi = 0$ to 2π. When $\phi = 0$, the input TOS directs all power from the input port (port 1) into the shorter delay path, and then the output TOS directs that light from that delay path into the lower-right output (port 4). As the value of $\phi = 0 \rightarrow \pi$, the magnitude of the group delay increases smoothly until reaching its maximum delay (most negative value) at $\phi = \pi$. This corresponds to both TOS switching all power into, and out from, the longer delay path. At all $\phi = k\pi$, $k \in \mathbb{Z} = \{\ldots, 0, 1, 2, \ldots\}$, the transmission is all-pass. However, as $\phi = 0 \rightarrow \pi/2$, this transmission drops, corresponding to the

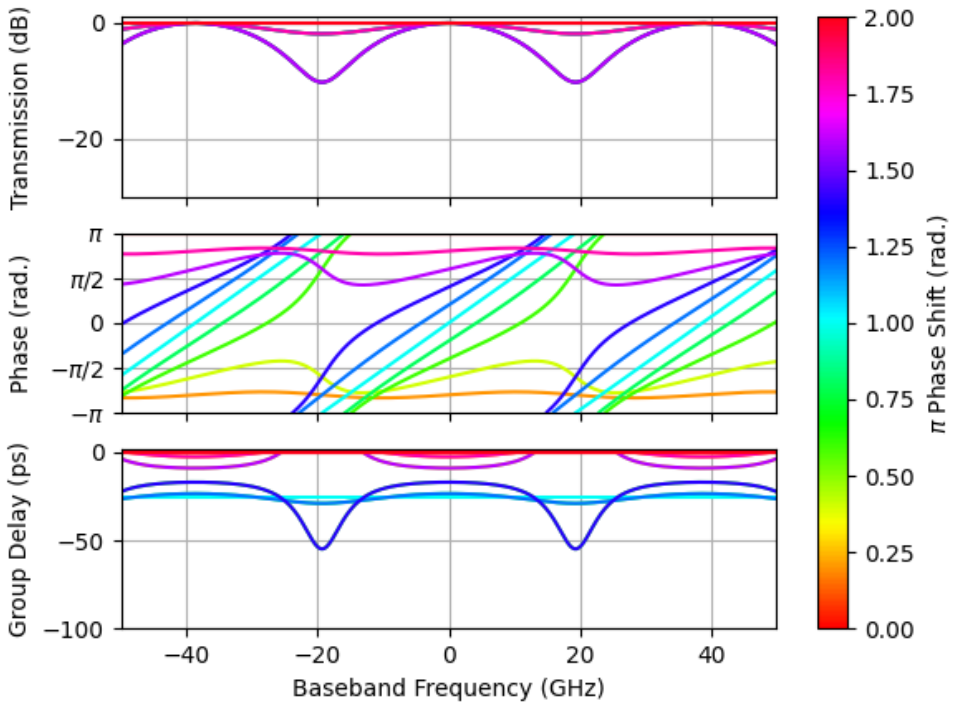


Figure 3. The transmission magnitude, phase, and group delay through the TOS delay line about the base-band center frequency.

FSR of the ideal MZI with the same ΔL. We can then identify that the TOS path delay line has a constant delay-bandwidth product for modulation about base-band centered on a transmission peak. In the particular example of Figure 3, N = 5000 and λ_0 = 1.550 µm. Then, the one-sided 3-dB bandwidth is 9.670 GHz (FSR = 38.683 GHz), and the maximum time delay change between switching states is 25.851 ps. In this scenario, the delay bandwidth product is 250 ps · GHz, or 0.250 s · Hz (a unit-less quantity). The energy lost in these bandwidth nulls is sent out of the auxiliary output port, $\overline{Out}$, AKA Port 3.

3.2 Switch with Feedback

We propose a modification to the architecture of an MZI-switched delay line, which restores all-pass behavior to the device. The light lost from Port 3 $\overline{Out}$ is sent through a feedback waveguide to the unused input Port 2. Subsequently, what was a 2×2 port black box is now a phase-controlled single input, single output black box. Under ideal conditions, all energy not lost to reflections or attenuation must exit through the output port, Out. The effect on the phase response is profound, which varies strongly as a function of the feedback waveguide length, L_{FB}. Although the magnitude of this transmission spectrum is unity everywhere, the phase response continues to meet a 2π phase jump at points corresponding to the equivalent ΔL MZI FSR. The transmission, phase, and group delay are presented in Figure 4. This provides for a tunable group delay without a corresponding transmission loss. However, the group delay response is not flat with respect to frequency. In effect, there is still a bandwidth limitation, and a wideband signal would experience some distortion passing through this device, rather than a TTD.

We can consider the resonant point within this device. As the input and output thermo-optic phase shifters vary simultaneously, all lines of phase meet asymptotically to the slope of the phase when $\phi = \pi$ at this resonant frequency. A narrow-band signal modulated about this frequency in the optical spectrum (by choosing an optical carrier centered on this point, or by shifting the optical spectrum by trimming the phase in one of the MZI arms) would experience constant group delay with respect to ϕ. However, sidebands of this frequency experience opposite changes in relative group delay, and the magnitude of this change is adjusted with ϕ. This theoretical device could perform the function of a delay compensation unit, creating a differential delay between the sidebands by pivoting the delay of the two sidebands about a constant value. However, a practical device experiences real attenuation loss. Assuming $2\,\mathrm{dB\,cm^{-1}}$ propagation loss for all waveguides, modified transmission, phase, and delay spectra are depicted in Figure 5. A detail view, limiting the phase shift ϕ from 0 to $\pi/2$, is shown in Figure 6. At a particular phase condition, the power-splitting fraction of the TOSs, the accumulated propagation phase, and the power loss transiting the feedback loop are balanced to produce more complete

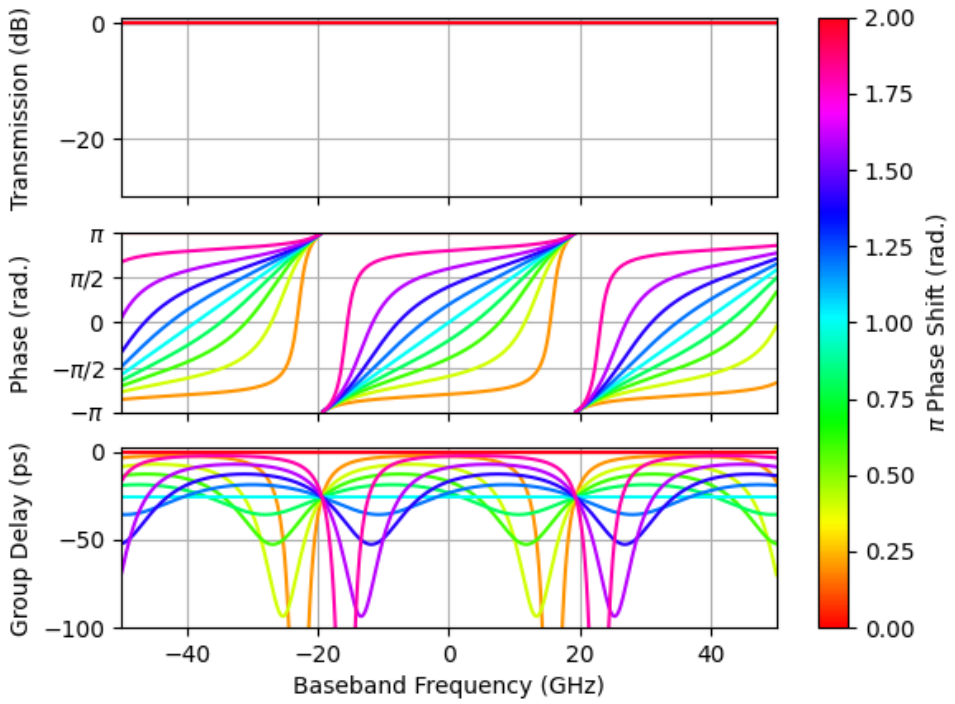


Figure 4. The transmission magnitude, phase, and group delay through the TOS delay line about the base-band center frequency. A feedback waveguide connects the auxiliary output $\overline{Out}$ with the upper-right input port. These simulated results represent an ideal case where waveguide attenuation is 0 $\mathrm{dB\,cm^{-1}}$.

transmission nulls through destructive interference. As will be present in many of these graphs, when transmission meets a deep null, the computation of the group delay loses its meaning, and the numerical computation can explode to a nonphysical value. A signal that is not detectable does not arrive with any meaningful or practical delay.

To gain further insight into this feedback-assisted switched delay line, we can consider its general netlist, and a few limiting cases, by choosing specific path lengths, 2×2 black box substitutions, and by breaking parts of the netlist. If the feedback path is disconnected, and the 2×2 black boxes are simple MMI or directional coupler devices, the netlist reduces to an Mach-Zehnder interferometer. Without the feedback path, when the 2×2 black boxes are TOSs, we recover the TOS delay line. Other netlists are also nearby in this configuration space, and their behavior can be instructive to

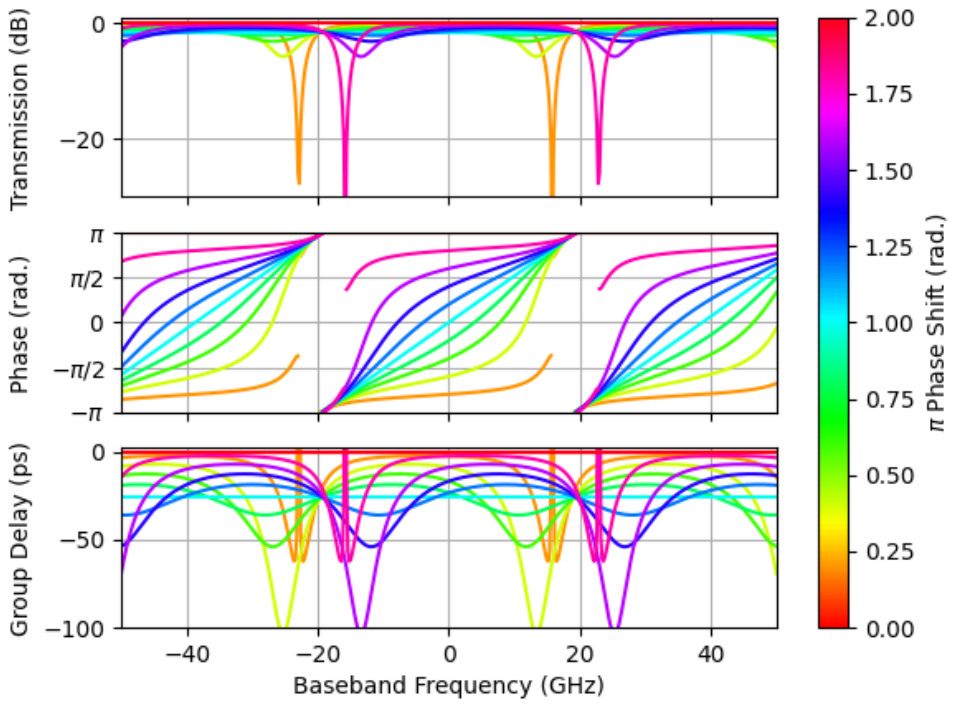


Figure 5. The transmission magnitude, phase, and group delay through the TOS delay line about the base-band center frequency. A feedback waveguide connects the auxiliary output $\overline{Out}$ with the upper-right input port. A constant waveguide attenuation of 2 $\mathrm{dB\,cm^{-1}}$ is assumed.

the overall operation of the family of netlists. If the 2×2 black boxes are directional couplers, and either the cross arm or thru arm of the interferometer is destroyed, the feedback path and the remaining MZI arm form a cross-coupled or bus-coupled ring resonator, respectively. When the length of the feedback path and the intact MZI arm are roughly equal, forming a symmetrically coupled ring resonator, the re-connection of the other MZI path with sufficient length can be thought of as a network bypass from the ring resonator's thru port, reconnecting to the ring resonator's add port. Then, all light enters the input port and exits the drop port. This configuration is entirely identical to the feedback-assisted switched delay line when the TOSs are replaced by point- or pulley-coupled directional couplers of the ring.

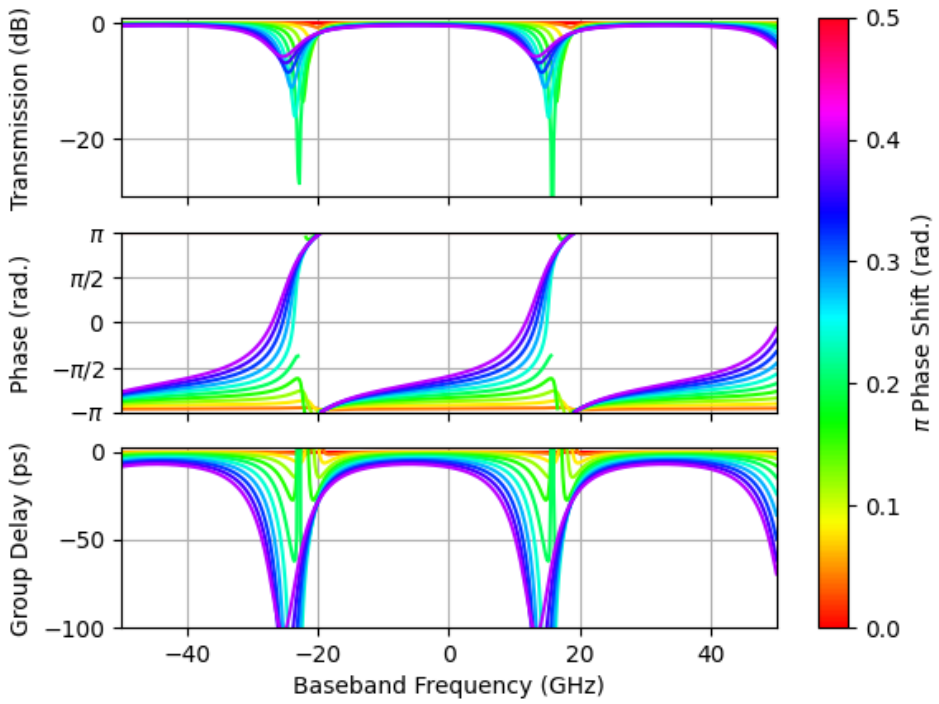


Figure 6. The transmission magnitude, phase, and group delay through the TOS delay line about the base-band center frequency. A feedback waveguide connects the auxiliary output $\overline{Out}$ with the upper-right input port. A constant waveguide attenuation of 2 $\mathrm{dB\,cm^{-1}}$ is assumed. Detail sweep to show the null transmission condition.

3.3 Wavelength Division Multiplexed Delays

The chromatic dispersion in a waveguide can be used to impart a time delay on the modulated signal by changing the operating carrier wavelength. We have previously explored such dispersive systems, typically using fiber Bragg gratings and their high differential delay near the transmission band edge.[3] There tends to be a finite bandwidth over which delay can be meaningfully accessed, as the magnitude of the delay is proportional to the transmission loss near the band edge.

As an alternative, a wavelength division multiplexed (WDM) system can be used to once again switch light through an appreciable path length to generate delay. One example is the arrayed-waveguide beamformer.[4] Another option is to use a ring resonator as a wavelength-dependent switch or filter. Light on resonance will take

one path, while light off resonance will pass through the ring's bus waveguide. The delay unit cell is depicted in Figure 7. Each ring in the sequence has an increasingly larger radius R, so that all N units have one resonance that falls within an operational free-spectral range.

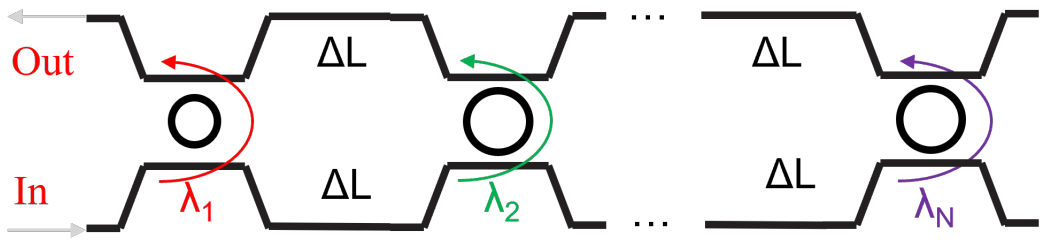


Figure 7. A cascade of ring resonators. For each choice of λ, the signal travels an increasingly longer path, adding an additional 2Δ L path length for each wavelength channel i from 1 to N.

4. Device Fabrication

Photonic integrated circuits were fabricated using the AIM Photonics foundry's Multi-Project Wafer (MPW) runs. Each run is assigned a unique identification number, as summarized in Table 1. The MPW runs utilized AIM's full active process, which includes integrated germanium photodetectors and optical edge couplers. A simplified schematic cross section of the full-active run is shown in Figure 8.

Beamformer concepts on 22-02A and 23-02A sought to demonstrate WDM TTD. Process variability was experimentally verified for the WDM styled chips, which drove the design decision to focus later designs at switched path-length architectures.

24-01A and 24-02A provided different implementations of thermally tuned path-length switched delays. The first chip, 24-01A, was designed to make use of a ring-resonator as a highly compact optical switch. The variability analysis from the previous chips indicated that this chip would need active electrical control of each ring to tune the system to its operating setpoint. This chip is designed to mount directly on a fan-in printed circuit board (PCB), with electrical connections made through wirebonding from the PIC top surface to the PCB. This assembly method was chosen to de-risk the second chip design, 24-02A, which is intended to demonstrate

the flip-chip assembly product offering from AIM Photonics.

Finally, an electronic interposer, 24-04E, was co-designed with the 24-02A chip to form a testbed for high-density electrical control and RF read-out from the PIC, while evaluating the flip-chip assembly product offering from AIM Photonics using a MZI-type switched path TTD unit, but placing it in a serial beamformer configuration. The electronic interposer layer stack is also depicted in a simplified schematic in Figure 9.

Table 1. AIM run identification.

ID	Type	Description
22-02A	Serial WDM TTD	30 Elements, 10 Rings per TTD Unit
23-02A	Serial WDM TTD	10 Elements, Spiral Cascade
24-01A	Serial Switched TTD	30 Elements, 3-Bit Rings per TTD Unit
24-02A	Serial Switched TTD	10 Elements, MZI
24-04E	Electronic Interposer	Flip-Chip BGA assembly with 24-02A

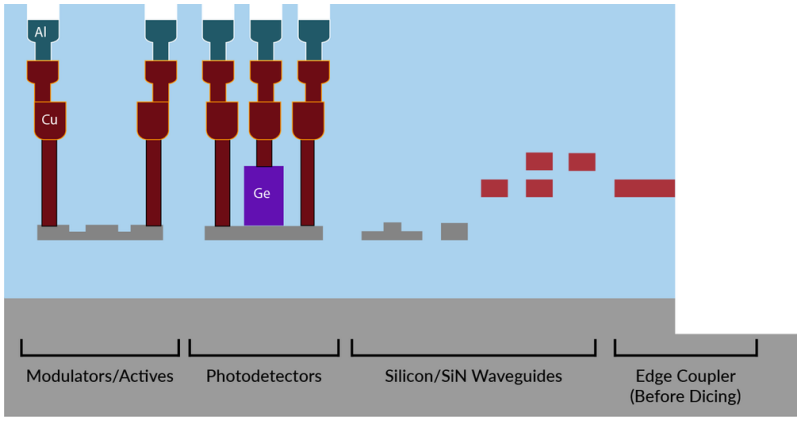


Figure 8. AIM Photonics Full Active Layer Stack.[5]

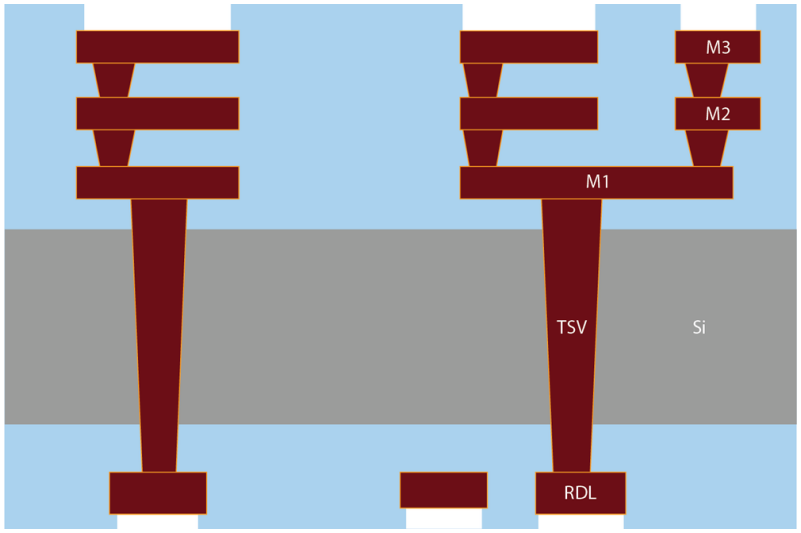


Figure 9. AIM Photonics Electronic Interposer Layer Stack.[6]

The first run, ID 22-02A, explored the WDM concept of Subsection 3.3. The schematic layout of the MPW reticle, alongside detail views of its power splitter and WDM ring resonator, is depicted in Figure 10. The intention of this run was to demonstrate the WDM time-delay concept. There are 30 TTD elements (30 outputs) that are serially connected using directional couplers as power taps to the optical output. The directional coupler elements were chosen from AIM Photonic's process design kit (PDK) and are available in two static power-splitting ratio designs: one providing a 1% power tap and one providing a 10% power tap. In order to obtain relatively equal power at each optical output, accounting for transmission losses and power lost at each previous power tap, it would be preferable for the power splitters to have a variable power ratio. With our PDK options limited to these two power tap ratios, the first 15 power taps were fixed at 1% power tap ratio, and the final 15 power taps used the 10% power tap ratio.

The spectral response of a single TTD element, made from a ladder connection of 10 WDM rings, can be measured independently for each of the 30 TTD elements by sending light inward from the N^{th} beamformer output. Two monitor photodetectors are available for use. One photodetector monitors the drop-response of the rings but has to pass through the power-tap coupler that comes before and after the TTD

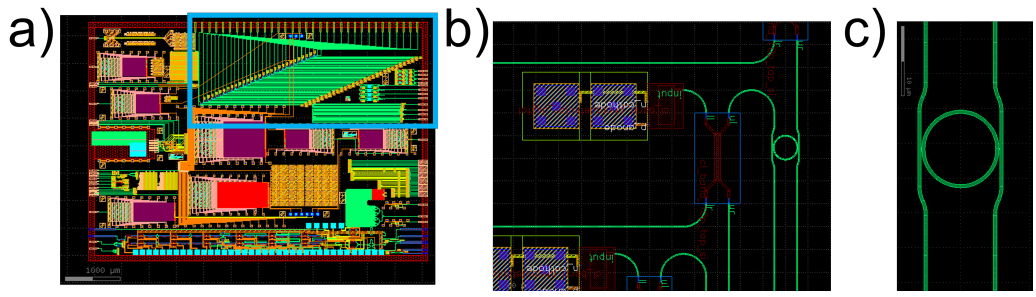


Figure 10. a) The layout of MPW run 22-02A, with blue-highlighted region containing 30 TTD units each made from a cascade of 10 WDM-separated ring resonators. b) Detail view of the power tap PDK cell, which comes in two power-splitting variations: 1% and 10% power-splitting ratios. c) Detail view of one WDM ring-resonator cell.

element to reach the drop-monitor photodetector. The second photodetector is placed at the opposite end of the TTD cell and captures all wavelengths that did not drop through the ring. The output of each photodetector is depicted in Figure 11. The top graph depicts the single-stage through response of each TTD cell versus wavelength. Five FSR groupings are visible for the wavelength range 1500 nm to 1580 nm. Each of the 10 rings in the TTD cell is designed with slightly increasing ring radii, which causes the individual response of each ring to be slightly shifted within the FSR. The background power is much higher for the highest ordered outputs because the power tap ratio is higher (10% instead of 1%). The bottom graph provides the corresponding drop port response, which passes from the chosen output through a power tap, the TTD, and the cross-response of a second power tap. Data is omitted for the first two TTD elements, since they have an auxiliary optical output instead of a monitor photodetector in these channels.

The measured ring response data reveals that the standard inter-component variability in AIM's process is high. Adjacent rings with different FSR within one TTD element are separated by 180 µm. Nearest-neighbor rings with the same radius, in adjacent TTD elements, are separated center-to-center by 78 µm. The operation concept of this device as a TTD beamformer relies on the ability of the first ring in each of the 30 TTD elements to have a shared resonant wavelength. The same requirement is true for every TTD element's n^{th} ring across all 30 TTD elements. Variations occur due to minute changes in the lateral etch resolution for each ring and are more strongly

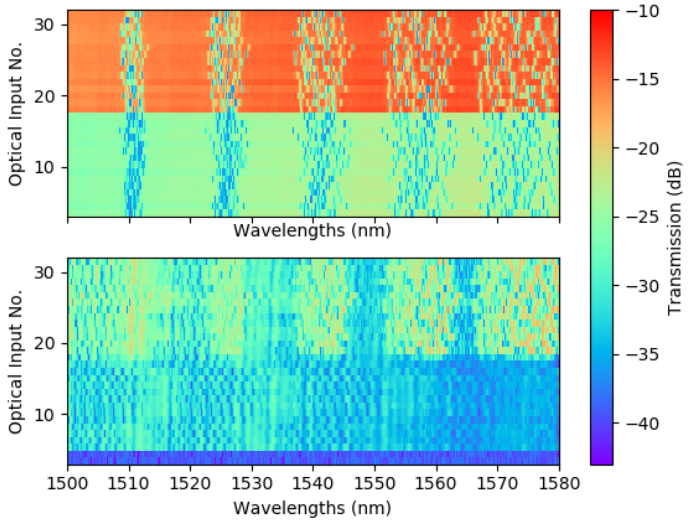


Figure 11. Measured transmission through a 10 ring x 30 stage beamformer.

affected by single-nanometer thickness variations across the land-area of the device. These effects are exacerbated by resonant devices like these ring resonators, by their high quality factor, Q. We can alternatively view Figure 11 as depicting the resonant wavelength variability, resolved over a $2\,\mathrm{mm}^2$ device footprint, for 10-ring radii with N=30 rings each. These measurements reveal that integrated photonic circuits implementing TTD through a WDM or resonant device approach will need some post-fabrication trimming to align the resonant wavelengths. Similarly, the entire chip was heated using a thermo-electric cooler (TEC). The through measurement response of one TTD element was recorded as a function of the background temperature. The spectra are depicted in Figure 12, which indicates that the rings are also sensitive to propagation constant changes induced by thermo-refractive index change, shifting the ring resonances uniformly by approximately $0.2\,\mathrm{nm\,K}^{-1}$.

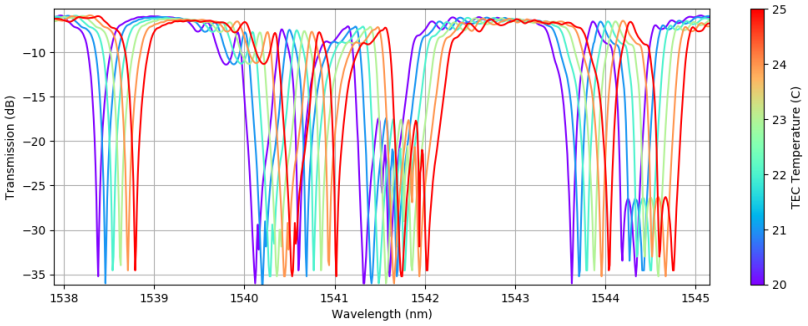


Figure 12. Spectral shift of 10-ring cascade as a function of substrate temperature.

5. Resonator-Switched Delay Circuit

The TTD unit cell and its placement within an array schematic are shown in Figure 13. The TTD cell is formed from a cascade of three highly compact path-length switches that are realized by a thermally tuned ring resonator. Activating the first ring will switch into the ring's drop response or accumulate $1\Delta L$ of additional delay. Activating the second ring will provide an extra $2\Delta L$ path length, and the third ring will provide $4\Delta L$. In this way, the TTD cell with three control bits should be able to access eight steering positions. The TTD unit cell is serially cascaded with a selected power tap directional coupler. A portion of the signal, delayed by the TTD unit, is sent through the power tap to that stage's antenna. The remaining signal continues through the power tap into the next TTD unit.

The layout of the beamformer is depicted in Figure 14. There are 30 TTD elements serially cascaded, each containing a three-bit path-length TTD unit formed from three independently controlled ring-resonator switches. Electrical wires that connect each heated ring resonator to electrical pads occupy most of the edge space on the chip. The path lengths are chosen so that $\Delta L = 200\,\mu\text{m}$. The heated ring resonator design uses the AIM PDK component cl_band_tunable_filter_si_lambda0.

A PCB was designed and fabricated using Sunstone Circuits, as depicted as a CAD render in Figure 15. Underneath the PIC (depicted with transparency to view the PCB) is a metal pad that makes mechanical and thermal contact with the underside

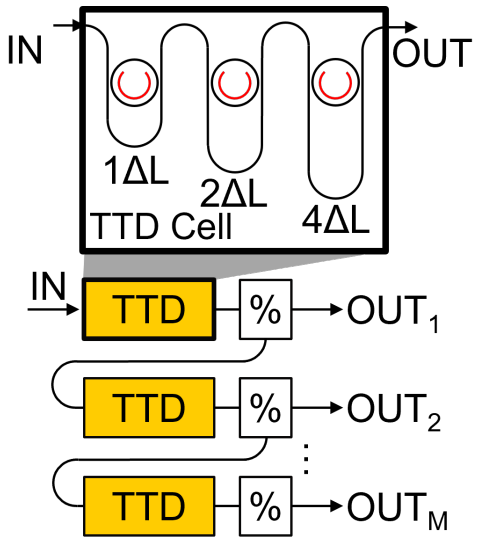


Figure 13. System block diagram with TTD cell exploded view. The signal enters at the IN port and accumulates a binary multiple of a design delay ΔL in the TTD component. A small fraction of the signal taps through an optical splitter (denoted "%") into a beamformer output. The majority of the signal transmits into the next TTD unit, accumulating additional TTD.

of the PIC using a thermally conductive epoxy (EPO-TEK H20E). This epoxy has a mix ratio by weight of 1:1, which is equivalently a volumetric mix ratio A:B of 1.51:1. It is baked at 90 °C in an oven for 3 h to cure. Metal vias connect to a similar metal pad on the underside of the chip, which is thermally bonded to a Thorlabs TECF2S TEC. An 0402-packaged thermistor, part number NTCG103JF103FTDS, is fixed to the top surface, next to the PIC. One of the two contact pads of the thermistor is physically shared with the landing baseplate of the PIC, so that they thermalize to the same temperature. Finally, a small anodized aluminum radiator is attached with thermally conductive tape to the underside of the TEC.

As a first characterization of this PIC design, the PCB only has 40 bondpads that run along one side of the PIC. The first pad is a shared ground for the ring heaters, while the remaining 39 pads can be used to address the first 13 TTD units (3 heated rings per TTD unit). A second larger fan-out board is used to interface the ribbon cable I/O with the TEC controller and a 40-channel Nicslab, Inc. multichannel SMU for driving the heaters. This PIC measurement setup is depicted in Figure 16.

A 32-channel, polarization-maintaining fiber array with 127-µm pitch between fibers

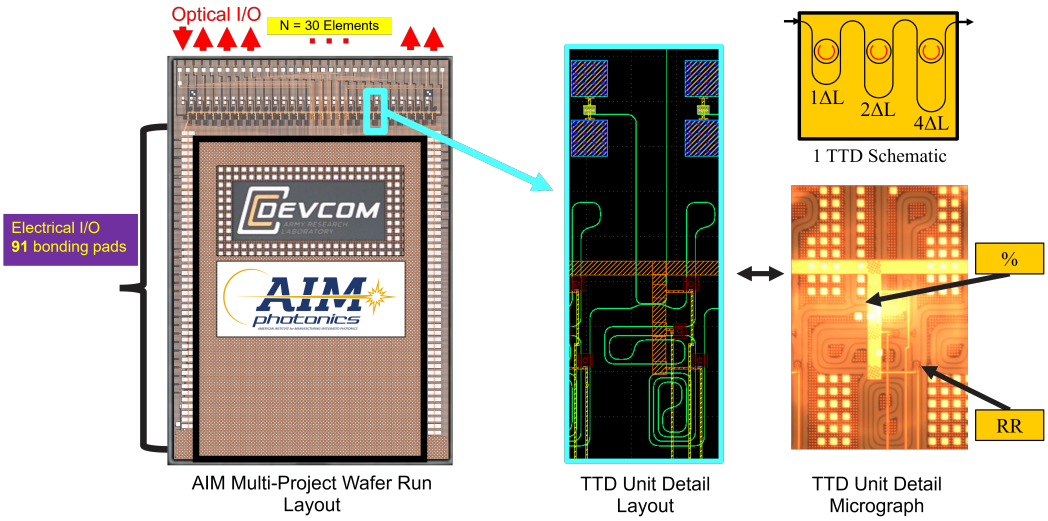


Figure 14. The fabricated layout of a 30-element beamformer on the 24-01A full-active MPW chip. Other MPW projects on the die are omitted. One TTD cell, composed of three independently tuned ring resonator switches, is depicted in the TTD Unit Detail view. A micrograph of the corresponding fabricated chip TTD unit is also shown, with one ring resonator "RR" and splitter "%" highlighted.

is aligned to the sample using two 5-axis micrometer stages. Light onto the chip is provided by the first channel, while the remaining channels provide optical read-out of each TTD unit stage through the variable power ratio directional coupler.

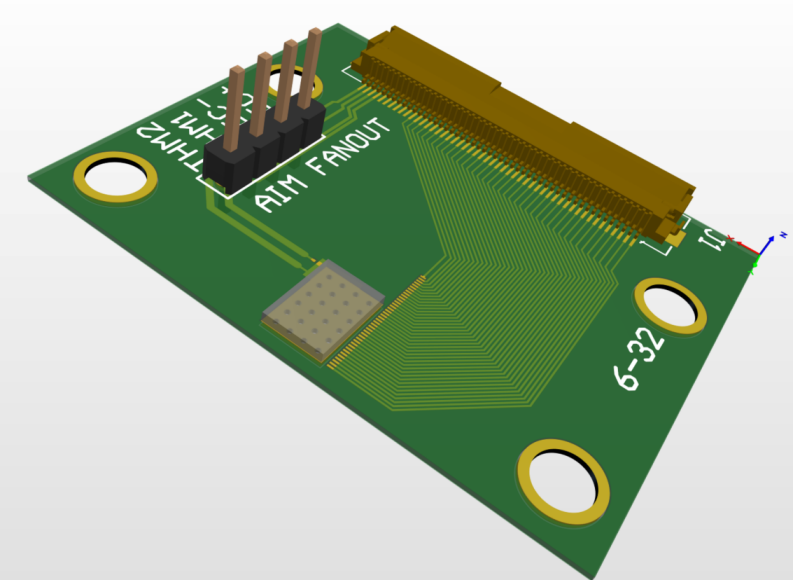


Figure 15. Interposer-less direct-mounting of PIC [24-01A] on PCB.

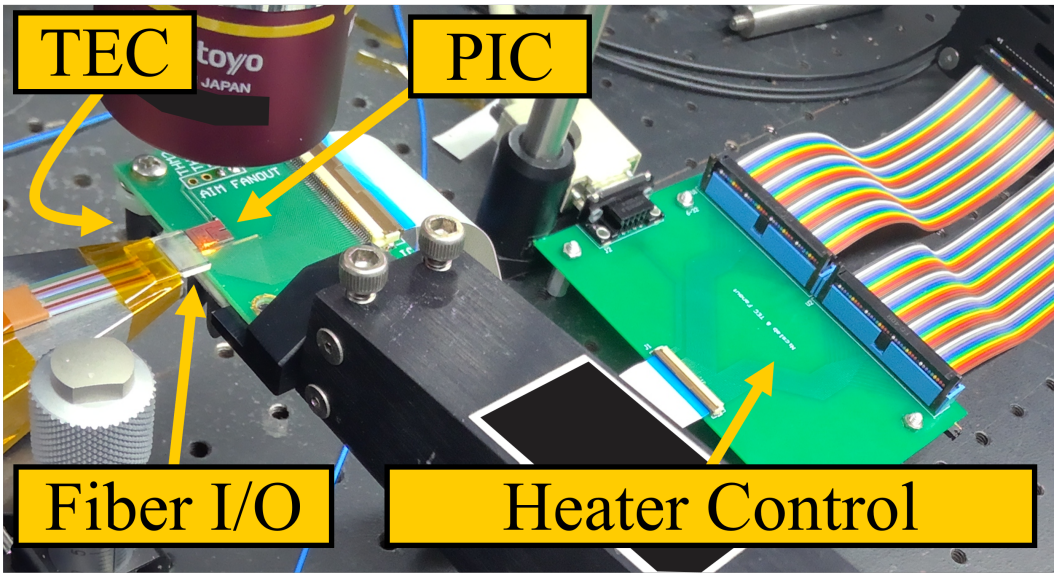


Figure 16. Wirebonded test assembly of a PIC connected to Nicslab multi-channel SMU and fiber array.

5.1 Variable Ratio Power Tap Design

The AIM Photonics PDK lacks an adjustable power tap directional coupler. Instead, users may only select from a fixed 1% and 10% power tap ratio. In a serially cascaded photonic beamformer, there is a need to optimize the amount of power tapped at each stage to maximize the amount of power available at each output and the amount of power passed to subsequent elements. For example, if the output powers along the array outputs are balanced according to a Chebyshev distribution, the sidelobe suppression of the resulting beam is maximized. In order to reduce the amount of thermo-optic control required on a beamforming chip, passive, static power taps are designed and targeted to give a uniform power output at each output tap in order to give maximum flexibility in the design of the electronic conversion stages that feed the antenna elements. The output coupling ratio expressed in decibels for each splitter in a 30-element beamformer chain is depicted in Figure 17. A ratio calculator was written in Python to compute the static coupling constants K for each stage of an N-element beamformer for any feasible power output distribution. In the uniform output power case, the insertion loss of each stage can be input into the calculator. The splitting ratios for uniform output power in a lossless circuit follow a power-law. Naturally, the final splitter in the chain is all-drop (100% or 0 dB) coupling ratio to the output and can simply be omitted. For a serial beamformer, this also allows for the identification of the maximum possible uniform power that each channel can output. With no insertion losses, each channel has 1/N of the input power. With insertion losses, the maximum power is found by iteratively running the calculator until the excess power (power not dropped into the final output of the array) is zero.

With the desired coupling constants K computed, a set of finite-difference time domain (FDTD) optical simulations were conducted for a parametric directional coupler design, with variable coupling gap and coupling region length. The simulation package used was Flexcompute's Tidy3D. The vector space of geometric variables was simulated to obtain a lookup table between physical layout parameters and the resulting coupling constant.

The parameterizable model layout of the directional coupler is shown in Figure 18.

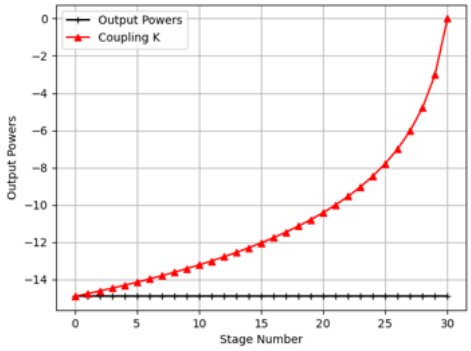


Figure 17. Target output coupling constants K for an N=30 element beamformer to achieve uniform output power.

The curves into and out of the coupling region strongly influence the initial coupling constant when the coupling length is 0 µm. The curves are fixed as Euler s-bends with radius 5 µm, which are paths with a constant rate of change of curvature and no curvature at the midpoint "flip" location. This allows the output waveguide to be modified to either bend with an east or north-facing output waveguide (similarly for the bottom east or south-facing) as shown by the dotted white line. This creates a versatile PDK library of couplers with different footprints to facilitate the smallest possible directional coupler within a particular circuit design. The gap at the flip location is approximately 1 µm, so that the coupling difference for designs with either flip orientation is negligible.

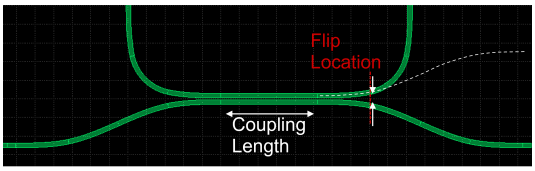


Figure 18. Physical layout of a parameterized splitting-ratio directional coupler. The inter-waveguide coupling gap and the coupling length vary to obtain the desired power tap ratio.

From previous AIM run data, the MPW process variation includes the assumption that layout masks undergo a real 10-nm process erosion. That is, a 500-nm-wide drawn waveguide on the silicon layer will erode to be 480 nm wide as-fabricated, and a coupling gap drawn 180 nm wide between two waveguides will result in a

200-nm gap as-fabricated. Wider coupling gaps are also more process tolerant, since the same process dilation represents a smaller percent error deviation in the design. Gaps of 200, 300, and 400 nm were considered to access a full range of coupling constants from 0 dB to −24 dB. Nominally, the directional coupler exchanges power with respect to coupling length according to $cos^2(x)$. However, the influence of the input and output couplers, which must taper inward to the coupling region, require a small correction factor in the model fit. This reduces the number of simulations that had to be performed while maintaining accuracy in the interpolation at small coupling lengths. The resulting data is shown in Figure 19.

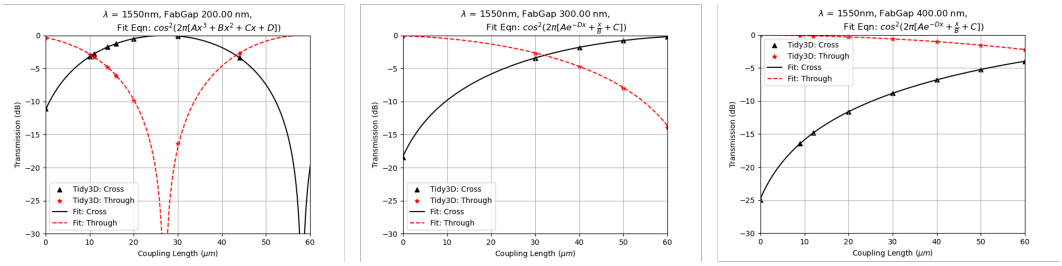


Figure 19. Curve-fits of coupling constant versus coupling length for various as-fabricated gap widths at 1550 nm.

In order to keep the footprint as small as possible, overlapping regions in the splitting ratio lookup table were created by varying the coupling gap. The final footprints can access the coupling constants range without requiring coupling lengths longer than 30 μm, as shown in Figure 20. For requested drop powers less than −10 dB, use a 400-nm gap for maximum fabrication tolerance and minimal footprint. For requested drop powers less than −4 dB, reduce the gap to 300 nm. For the final output power taps that require higher than a −4-dB ratio, the highest variability 200-nm gap must be used. An equivalent device at 300-nm gap would require a coupling length that is nearly twice as long (60 μm versus 30 μm).

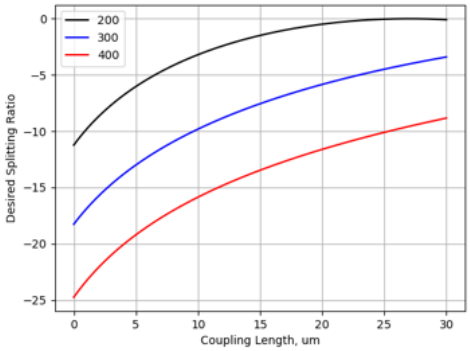


Figure 20. Final splitting-ratio to coupling-length lookup table for selected coupling gap widths of 200, 300, and 400 nm.

5.2 Ring Resonator Characterization

The optical response of the tuned ring resonator TTD cascade was characterized. The Nicslab source measurement unit (SMU) can sweep across one or multiple channels simulataneously and record the current draw as a function of applied voltage across each heater. The I-V curve for a selection of the ring heaters is depicted in Figure 21. In agreement with the AIM Photonics PDK specification, the nominal resistance of each heater is approximately 200 Ω. As more current flows through the device, joule heating occurs. As the local temperature increases, the silicon exhibits a self-limiting positive temperature coefficient, and the resistance increases.

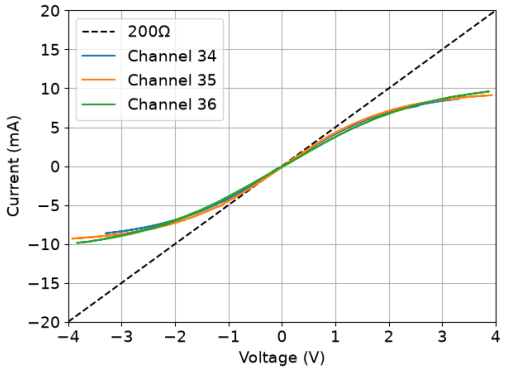


Figure 21. Ring heater I-V curves referenced to the PDK reported 200 Ω nominal resistance.

Without on-chip gain, the serial beamformer will be limited in the number of elements

it can cascade through while still providing adequate and uniform output power. So, it can be convenient to simply increase the input optical power to provide proportionally higher output power. However, a photo- and thermo-refractive index change due to high local optical power creates a non-linearity within the device response. When a swept laser source has its lasing wavelength approach the resonance of one of the silicon ring resonators, the optical field buildup can cause the ring to walk-off resonance. During a wavelength sweep, this walk-off action appears as an apparent distortion to the Lorentzian lineshape of the resonator's response spectrum. Likewise, the wavelength of the source laser can be held constant, and the ring resonator's resonance can be swept onto the laser by heating the ring. The integrated doped silicon heater is located within the inner radius of the ring resonator, and a portion of the evanescent optical field within the resonator overlaps with the heater. This overlap leads to a small amount of absorption in the ring. It was observed that optical power that overlapped with the doped heater caused the creation of electron-hole pairs that could then be swept by the heater's applied voltage in the form of a slight increase in current. Calibrating away the heater current response when the optical light is off, the excess induced current as a function of the heater voltage is depicted in Figure 22. The excess current is only detectable when the ring is nearly resonant, due to the buildup of field within the ring near resonance, and hence, more absorption in the heater. The excess current is measured as a very weak (tens of microamps) signal that can be used in a sensitive control system to identify when a ring of interest, independent of other rings in the system, is resonant at the source wavelength. This general observation can be useful for the control of any resonant silicon photonics circuit with doped silicon heaters. This excess photocurrent is directly proportional to the field buildup within the particular ring resonator, so it also provides a measurement of the optical non-linearity, shown by the asymmetric response as input optical power exceeds 8 dBm.

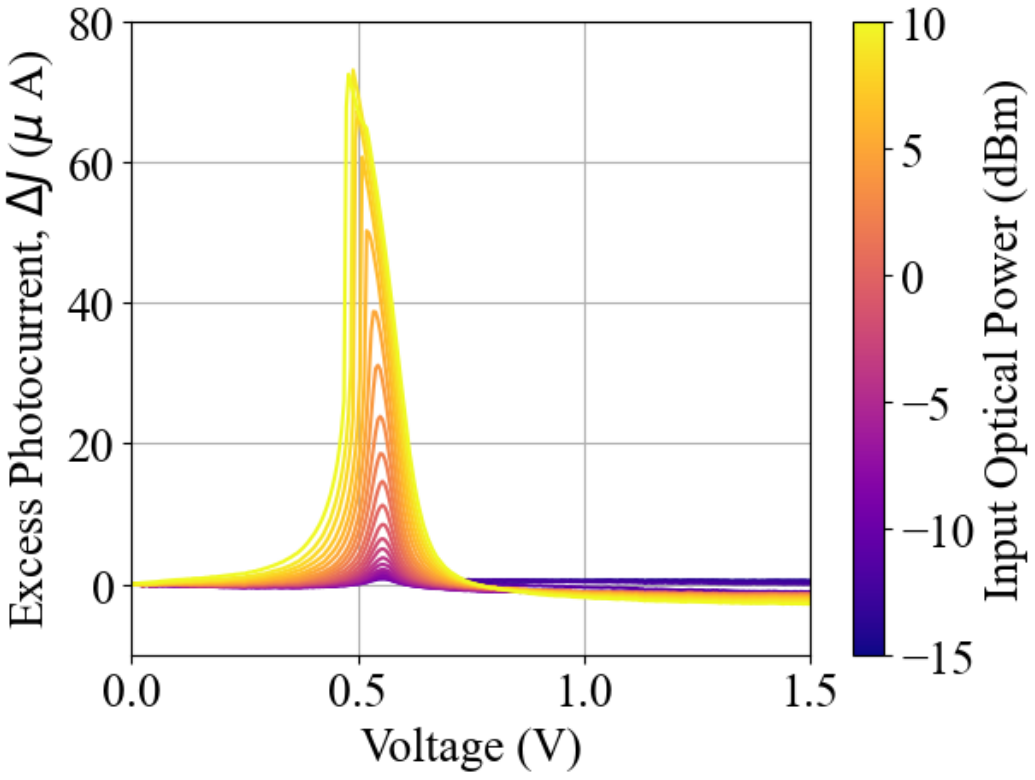


Figure 22. Excess current in ring resonator's heater due to applied optical power.

5.3 Catastrophic Optical Damage in AIM Platform

One AIM photonic sample experienced a catastrophic device failure that is recorded here. Input laser light not exceeding 20 dBm was incident onto the sample through an edge coupler. Other recent literature report appreciable two-photon absorption in silicon for greater than 15-dBm power.[7] Due to the facet losses, the optical power coupling into the waveguide should not be high enough to cause damage to the silicon waveguiding layer. During alignment of the optical fiber, the coupled power into the output fiber and photodetector dropped instantaneously, such that light was no longer coupling into the output waveguide. On inspection of the chip in an optical microscope, the first ring resonator in the path from the input fiber was blackened. The material has not been identified. Figure 23 depicts an undamaged and damaged ring resonator, alongside the view through the short-wave infrared (SWIR) camera. The color change was immediate and permanent. We have observed a similar phenomena

once before, where a combination silicon and silicon nitride waveguide edge coupler/ system of tapering waveguides surrounded by oxide immediately became blackened (only in the space occupied by the waveguide) and stopped effectively transmitting light. The blackened material is underneath the overhanging metal layers, suggesting that it is either in the silicon layer itself, an intermediate material layer, or the heater via layer.

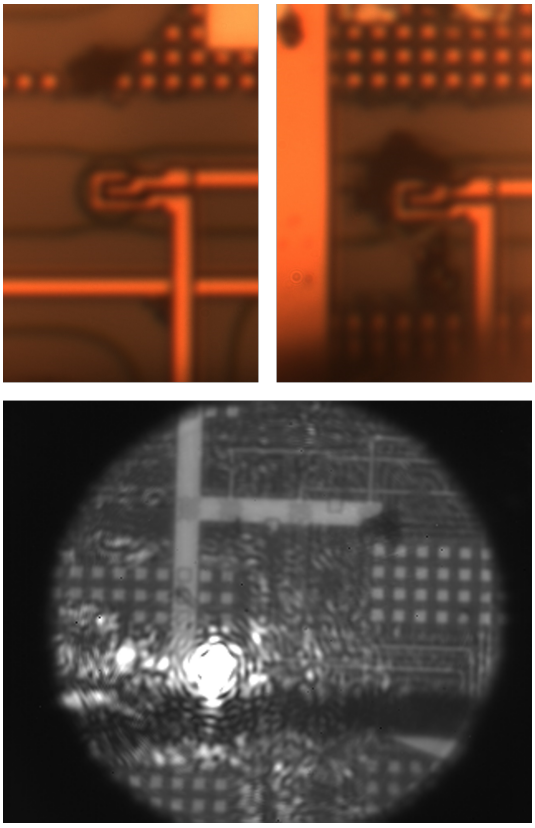


Figure 23. Catastrophic device failure. Blackened material formed on the first input ring resonator on this silicon die. (Top Left) Standard AIM Photonic PDK ring resonator. (Top Right) Ring resonator after damage. (Bottom) SWIR image of light ejecting out of the damaged ring.

A second AIM chip with the same PCB assembly design was constructed to continue characterization.

5.4 Tuned Ring Resonator TTD Unit

Next, the response of the tuned ring-resonator TTD unit was characterized. The initial goal of this effort was to identify and calibrate the resonant wavelength of each

path-length bit-switch to set them to be co-resonant. That way, the voltage required to place any subset of switches into a resonant state could be retrieved from a system controller and the delay through all eight bit-switching states could be measured.

First, the linear transfer function of the system was obtained using a Luna Technologies optical vector analyzer (OVA). The experimental setup is detailed in Figure 24. The Luna OVA sends a broadband time-domain pulse through the system and measures the polarization-dependent time domain response at the optical output. It uses this information, and applies a Fourier transform, to obtain an optical Jones matrix, which completely characterizes the linear polarization-dependent response of the system across the C-band. A temperature controller is used to keep the PIC at a constant

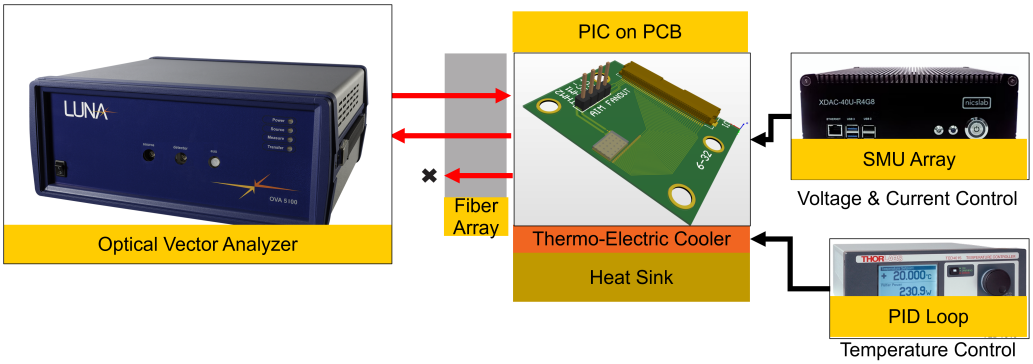


Figure 24. Linear transfer function measurement using a Luna optical vector analyzer.

background temperature of 20 °C, and the Nicslab SMU array is used to sweep the voltage applied to a subset of heaters. The absolute transmission loss through these devices is about −28 dB. Of that, approximately 11 dB is due to the 5.5 dB/facet insertion loss on-and-off the chip using the fiber array without any index matching oil, or numerical-aperture matching lenses on the fiber array tip. Most of the rest of this loss is intentional. For a 30-element beamformer with ideal power taps to provide equal output powers, each output would sit around −15 dB, with 2 dB remaining unaccounted for possibly belonging to insertion losses in the TTD element. A small waveguide width mismatch at each PDK ring input and output between the PDK specified width and the drawn-waveguide width (of only a few nanometers) is present in this particular reticle mask. To correct for this mismatch in subsequent runs, we

have adopted a GDSFactory tapeout methodology to catch these small waveguide mismatches during the tapeout design review. The resulting output spectra as each individual ring in the first TTD stage is heated is depicted in Figure 25. Both the large dip in the spectrum and the ripple across the spectrum are identified with various weak Fabry-Perot resonances that exist in cavities formed from reflections off of these specific fabricated waveguide width errors at the input and output of each PDK ring cell.

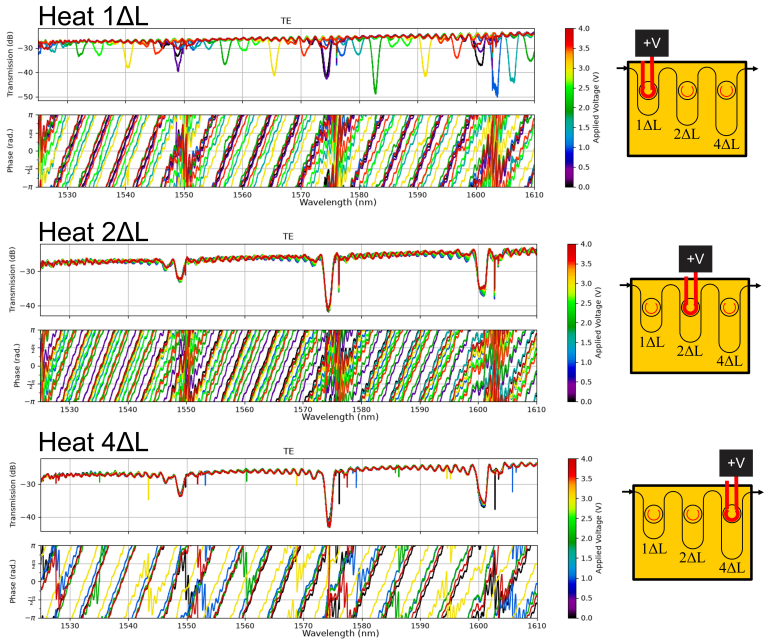


Figure 25. Measured transverse-electric polarized transmission and phase response of one 3-bit tuned-resonator TTD element. A small graphic on the right depicts where the applied voltage is being swept for each transmission and phase plot.

Additionally, the system was attached to instrumentation to allow for the direct measurement of an RF signal time-delay in a 40-GHz oscilloscope. The system diagram is depicted in Figure 26. A tunable laser, Santec TSL-570, sets the carrier wavelength. A commercial off-the-shelf modulator (Optilab IML-1550-40-PM-V transduces the input RF sinusoid from a Keysight E8257D signal generator onto the optical carrier. A polarization-maintaining erbium-doped fiber amplifier (Thorlabs EDFA100P) amplifies the signal to compensate for insertion losses and to increase the end-to-end RF gain. A fiber array couples light into the PIC and retrieves two

output signals. The first output signal represents the undelayed reference signal and couples out from the first power tap. The second output signal passes through the first delay unit before being output from the second power tap.

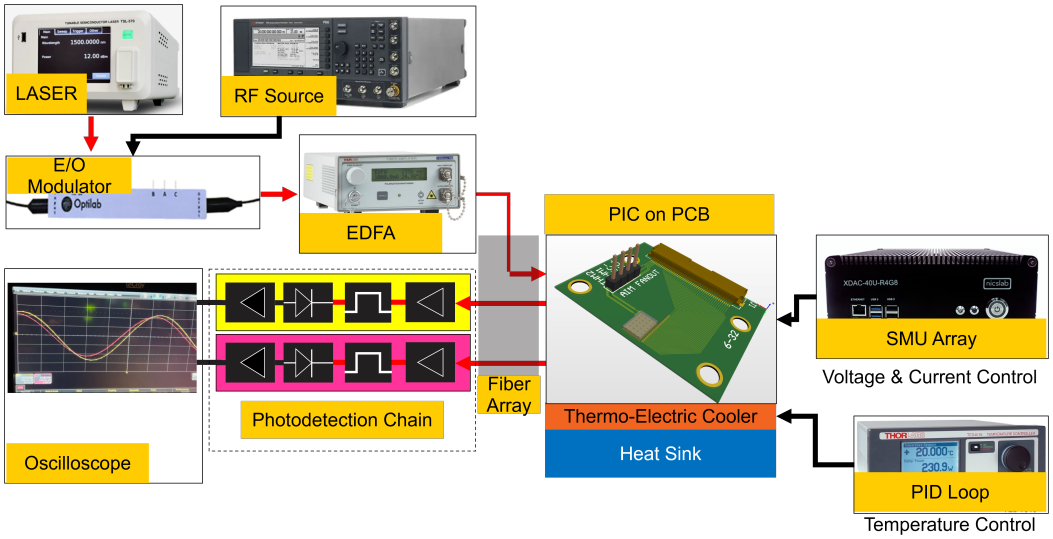


Figure 26. Schematic diagram for time-delay oscilloscope capture.

6. MZI-Switched Delay Circuit with Interposer

A beamforming chip was designed with the goal of testing the ability of AIM Photonics to integrate a PIC with its electronic interposer technology. By exercising this fabrication option, we expected to obtain a PIC demonstrator to evaluate the signal quality across the PIC-to-interposer interface so that iterative designs could be made to optimize electronic control and RF signal I/O to the PIC. This work is necessary to realize the concept of a PIC beamformer, which will require a dense interconnection of control and calibration, optical, and RF signals. Already, the previous beamformer was limited in silicon footprint by its electrical fan-out. By switching to a flip-chip on interposer design, electrical fan-out can be read out through a ball-grid array (BGA) footprint. This choice of electrical interface also lends itself to mass manufacture, as the BGA interface can be seated on its interposer through a solder bump process that is higher throughput than wirebonding directly from the top surface of the PIC to a breakout board. Additionally, we anticipate that moving to the higher integration density of the interposer, and using its through-silicon-via

(TSV) to interconnect the PIC's RF output signals to a fan-out PCB, will improve RF signal integrity.

The proposed material stack-up is illustrated in Figure 27. The 8 mm^2 BGA interfaced MPW PIC 24-02A has its top pads formed in a modified process that introduces copper into the aluminum pad alloy during deposition. The addition of copper to the pad material is meant to facilitate better adhesion of the chip-to-chip interface. Originally, this chip was intended to test the AIM Test, Assembly, and Packaging (TAP) copper-bump process, but the first chip lot available for test has a lower-risk bump plan that uses a solder-ball process for both the PIC-to-interposer and interposer-to-PCB. The MPW PIC is flipped upside-down and its top surface is connected through this bump process to a matching BGA landing on the top surface of the interposer. The interposer features three top-side metal layers and one redistribution layer (RDL) on the bottom side, connected with TSVs. The schematic layout of chip 24-02A is depicted in Figure 28. The BGA pads are indicated by 100- × 100-µm blue squares with an 80-µm-diameter circular passivation opening centered on each square pad. The pad-to-pad pitch is 180 µm.

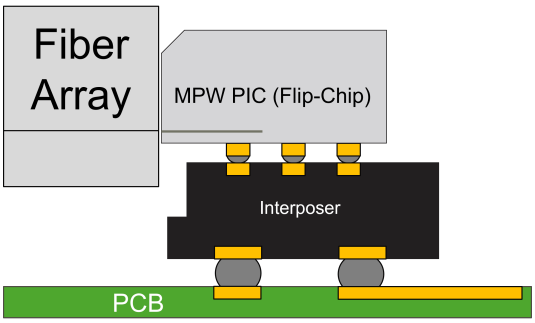


Figure 27. Side view of the planned PIC + interposer + PCB stack.

The MPW layout also features a deep pocket in the lower-left corner of the floorplan, which is meant for a separate heterogeneous laser attach project. Although not exercised in this program yet, attempting to integrate this chip with the interposer should reveal compatibility of these deep-trench integration techniques, which prevent some BGA pads from being able to contribute to the mechanical stability of the chip-to-chip attachment.

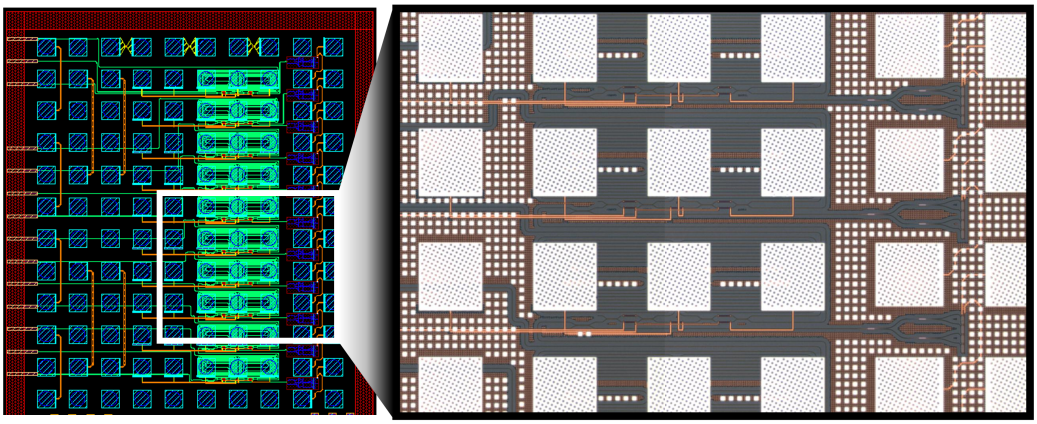


Figure 28. Chip 24-02A schematic and fabricated layout. Left: The 10-element MZI-type TTD serial beamformer circuit is shown in schematic view. Right: A detail view of arrayed bond pads intended for flip-chip bonding to the 24-04E interposer, above a few of the TOSs and spiral delay lines that form the TTD elements.

To maintain clearance in the stack-up between fiber array, MPW PIC, and interposer, it is necessary that either a lidless fiber array be used (not pictured) or that post-fab processing be conducted at AIM TAP to remove the trench lip that surrounds the AIM PIC facet. In the present implementation, only one optical input is used to drive the serial phased array. The other optical ports of this chip are used to individually address each TTD element, which is included to help troubleshoot and characterize the PIC.

Each TTD element is formed by a switched-path MZI design with path lengths of 0.050 and 8.85 mm. The long path forms a two-part spiral to fit within a 125- × 440-µm footprint. An AIM PDK analog photodetector with a nominal bandwidth of 34 GHz is attached at the output of each TTD element using the same variable splitting ratio power taps described in Subsection 5.1.

The interposer design schematic is depicted in Figure 29. This design, 24-04E, has a footprint of 12 mm × 13 mm. The layout of 24-02A is superimposed in the red outline on the left center of the image, depicting the alignment and placement of the flipped-chip above the interposer. DC electrical output for each TTD element's TOSs and MZI phase shifter is accessed through the north and south sides of the chip, which distribute through the TSVs to a 420-µm-diameter circular RDL pad

with a 400-µm passivation opening. The bottom RDL pads have 1-mm pitch.

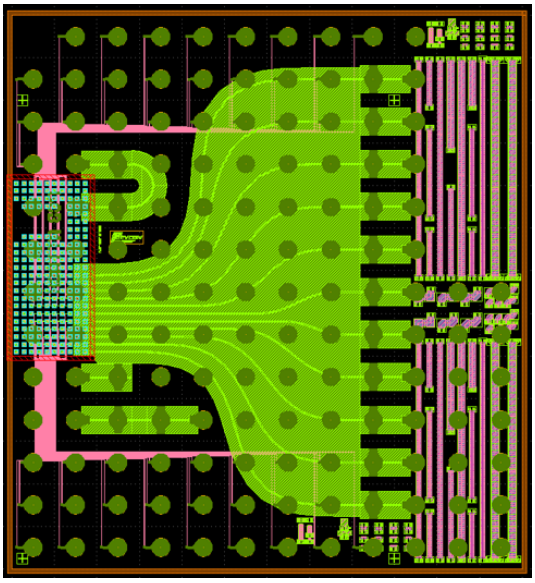


Figure 29. Schematic view (X-ray) of AIM chip 24-02A (red outline) flip-chip attached to the interposer 24-04E.

The serial beamformer on this demonstration platform has 10 concatenated MZI-type TTD elements. Each of the 10 output photodetectors fan out across the top surface of the interposer through a ground-signal-ground coplanar waveguide (CPW). AIM Photonics provides a PDK of predefined CPW dimensions for each layer to obtain a 50 Ω impedance. The photodetector outputs fan out across the top-level M3 layer. The other two top side metal layers, M2 and M1, are used to connect to the TSV and to route the DC heater control signals from the BGA contacts.

6.1 Device Characterization

A number of administrative and process delays occurred within the AIM Photonics foundry during the fabrication of the 24-04E electronic interposer run, leading to a significant 14-month delay in obtaining the interposer. Its companion chip, the 24-02A full active run, did not suffer from any anomalous fabrication delays, and was delivered on time. Some characterization of the 24-02A chip was performed on the full-active chip alone, without any assembly to the unavailable interposer. However, the two chips were co-designed to be flip-chip attached together, and accessing and driving the high-density BGA arranged pad-pitch on top of the 24-02A die with

probes was infeasible. Individual devices were probed in order to characterize them. The response of the on-chip AIM PDK photodetector to input optical light at various reverse bias voltages is depicted in Figure 30. At a nominal 1V reverse-bias, the response is linear until approximately 9 dBm of input optical power.

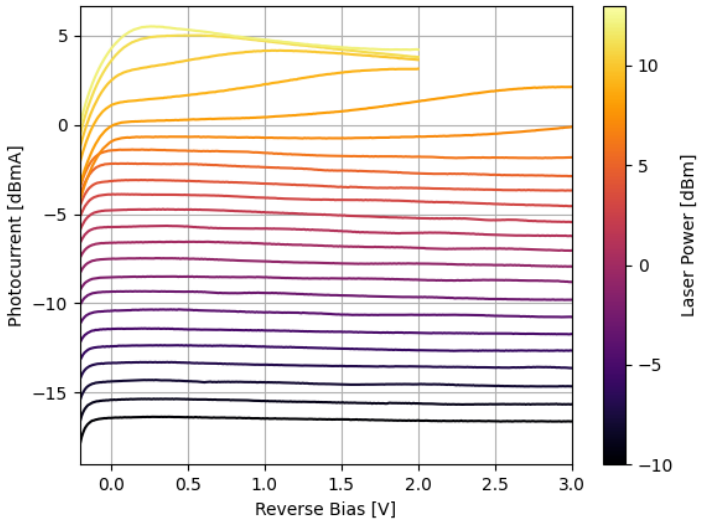


Figure 30. On-chip AIM PDK analog photodetector response versus reverse bias voltage as a function of input power.

The heater controls on a single TTD element were then swept to characterize the operating point of the device. The MZI-type TTD element has three heaters: one to actuate the input TOS, one for the output TOS, and one for the phase control of the short arm of the MZI. The output of the system over a dense dataset of system inputs was collected, and a cut line through that dataset is depicted in Figure 31. The left-most image depicts the simulated response when the MZI heater is unheated, and the two TOS heaters H1 and H2 are independently manipulated. The right-most response depicts the corresponding measured output power, which shows good agreement with theory. The axes are mapped to align the physical current value, which provides a π phase shift, with the corresponding simulation current. This dataset is 3D, and included data taken at each input/output TOS heater while the MZI heater current sweeps. A video of this dataset is available upon request. Unlike in the simulation, the measured data only achieves its highest power to the output

when both outputs are switched on, but not equally. This is seen in the measurement data as a bright spot on the high transmission iso-line, slightly off-center from the main diagonal. This indicates that the maximum switching state for each TOS occurs at a slightly different voltage due to fabrication variations on-chip. The input and output TOS are 150 µm center-to-center on the chip layout. Figures 32 and 33 explore specific cutlines through this configuration space, depicting the output photocurrent of the TTD MZI device. Each curve provides a top graph where the sweep is taken from left-to-right (heating the heater element) and the bottom graph where the sweep is taken right-to-left (the heater is cooling). There is some thermal loading effect here from not allowing the system to fully thermalise between datapoints. This demonstrates that the reconfigurability of the delay line is limited by the thermal switching speed. The MZI extinction ratio is not equal for the forward and backward sweep. This is because the heat from each TOS thermalizes the surrounding oxide material, which antagonistically heats the two MZI arms slightly and unequally. This drives the system off of the ideal deconstructive interference setpoint, reducing the extinction ratio. Careful thermo-optical control of the device and additional thermal shielding between components may be necessary to improve the agility and ease of control of the MZI TTD unit cell.

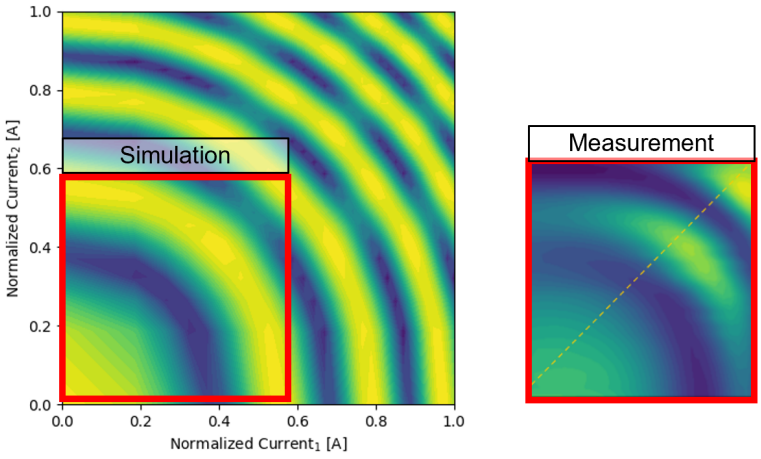


Figure 31. Transmission through one TTD MZI as a function of input and output TOS heater current: (left) simulated response; (right) measured response with axes rescaled to provide a direct comparsion.

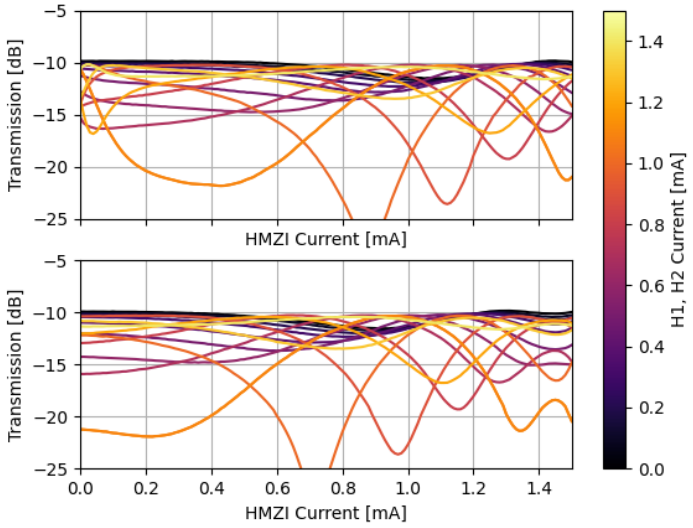


Figure 32. Output photocurrent as a function of MZI heater sweep. Each curve represents a different switching state configured by the input and output TOS heater settings (H1 and H2) co-varying.

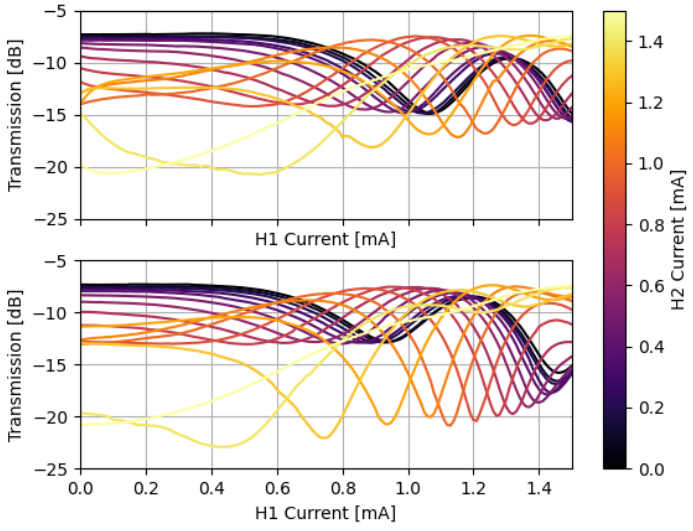


Figure 33. Output photocurrent as a function of the input TOS heater current at select output TOS heater current switch states. The MZI heater is undriven.

6.2 Wideband Phased Array Antenna

Work also began building PAA hardware with which to co-integrate with the PIC beamformer so that the system can be demonstrated with a far field test of beam steering within an anechoic chamber. The system requires a fan-out PCB to distribute the RF signals from the PIC Interposer assembly into a form factor that is compatible with the feedline pitch of the PAA. This PCB will be directly solder-bumped to the underside RDL of the interposer using a 1-mm pitch BGA footprint. The PCB will also provide surface mount bias-tees to reverse-bias the PIC integrated photodetectors, and, optionally, amplifier monolithic microwave integrated circuits for application-specific power requirements. This board will route the delayed signals to a transmission-mode PAA. Tidy3D FDTD simulations were conducted using the RF modeling toolbox to optimize the CPW dimensions for 50-Ω impedance on the PCB. Computed impedance across the operating spectrum is depicted in Figure 34. For an FR4 (permittivity 4.4) board with 1-mm thickness from the CPW to the embedded ground plane, a 3-mm-wide strip with 0.5-mm-wide space to 2-mm-wide ground lines produces a 50-Ω impedance.

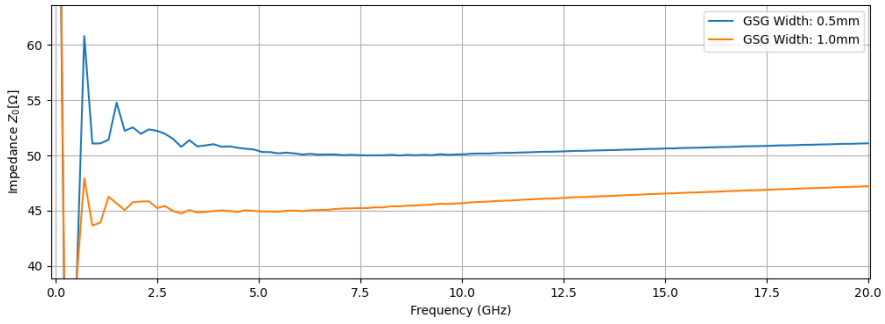


Figure 34. RF simulations of transmission line impedance versus trace width on the fan-out PCB.

To demonstrate the beamforming of signals using the AIM MPW PIC on interposer, a wideband Vivaldi-type antenna was designed in collaboration with C5ISR's Antennas & Resilient Communications Branch to interface to the PIC + Interposer + PCB stack. Then, the antenna was manufactured using C5ISR's Prototype Integration Facility (PIF). A CAD description of the 30-element antenna is depicted in Figure 35,

alongside simulations of a single broad antenna emitter and the narrow beam profile when all emitters are properly time delayed.

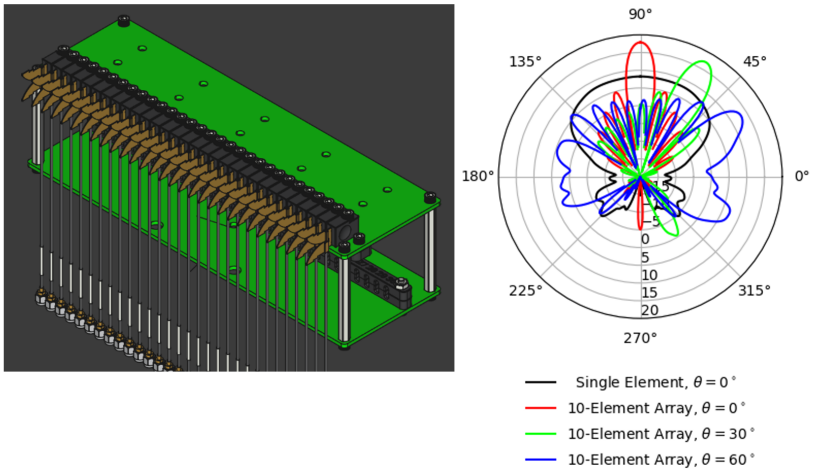


Figure 35. (Left) 30-element 10-GHz Vivaldi-type antenna array with coaxial feeds. Fabricated at C5ISR's PIF (March 2026). (Right) Simulated beam for only 10 driven elements at selected steering angles.

The resulting prototype antenna with assembled RF feedlines is depicted in Figure 36.

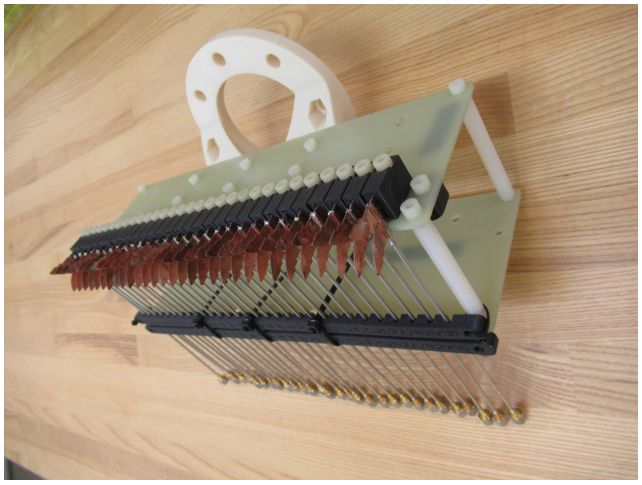


Figure 36. C5ISR PIF fabricated antenna with RF cable feedlines.

Initial acceptance tests were conducted by the C5ISR Antennas & Resilient Communications Branch. The measured gain profile for the emitter in the center of the array

is depicted in Figure 37. It shows good agreement with the simulated single-element emitter profile. The beam width of a single antenna spans approximately 120° FWHM, which lends itself to beamforming over a wide field of view. The relative phase error of each feedline was also measured within the assembly. These errors will be compensated by the PCB in the future. The voltage standing wave ratio for each antenna was also characterized, and found to be less than 2.5 for each element.

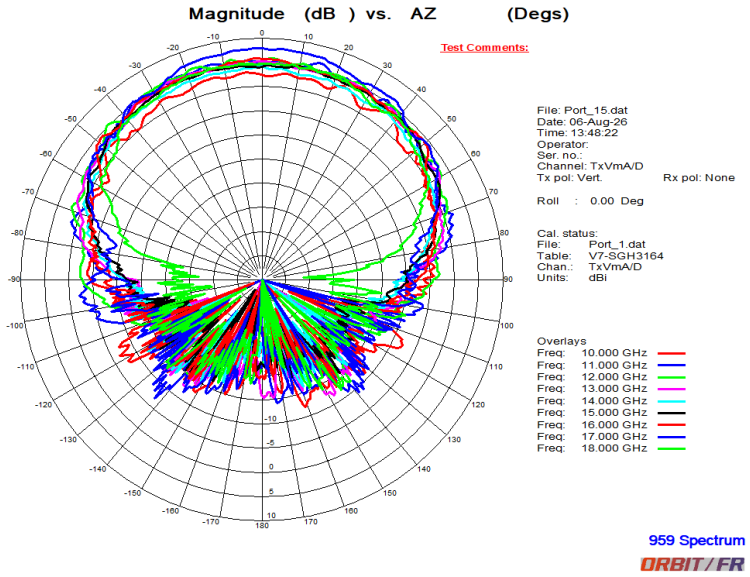


Figure 37. Azimuthal gain profile for the centered (Port 15) emitter. Vertically polarized.

7. Conclusions

This report represents a snap-shot of work-in-progress towards integrated photonic RF beamforming. These PICs are able to be modeled comprehensively through transfer-matrix methods, alongside FDTD simulations for sub-component design. A range of process-calibrated power tap directional couplers were successfully fabricated, which will continue to be a useful sub-component in future arrayed PIC designs. The resonator-switched TTD architecture presents a trade-off between providing significant phase-control near resonance with a penalty of wide process variation that requires complex thermo-optic correction. Control methodologies are limited by the density of electrical inputs and outputs that can fan-in and out of the PIC. Electronic interposer technology provides a promising mass-manufacturable method toward

densely integrated PICs alongside electronic control. Although delayed within the scope of this report, our exercise of the foundry interposer offering has improved their processes and turn-around time. Future work will seek to complete the integration of the PIC, interposer, PCB, and PAA. The PIC-driven antenna will be tested in an anechoic chamber. Exercising this assembly process will better position our photonic circuit industrial base to fabricate and assemble future RF-photonic PIC systems.

8. References

1. An T, Liu L, Han C, Zhu S, Jiang Y. A review of research on optical true time delay technology. J Eur Opt Society-Rapid Publ. 2025;21(1):2. https://doi.org/10.1051/jeos/2024046
2. Melati D, Waqas A, Mushtaq Z, Melloni A. Wideband integrated optical delay line based on a continuously tunable Mach–Zehnder interferometer. IEEE Journal of Selected Topics in Quantum Electronics. 2018;24(1):1–8. https://doi.org/10.1109/JSTQE.2017.2723955
3. Zhou W et al. Developing an integrated photonic system with a simple beamforming architecture for phased-array antennas. Appl Opt. 2017;56(3):B5–B13. https://doi.org/10.1364/AO.56.0000B5
4. Tyndall NF et al. Photonic integrated circuits for microwave photonics in a 300-mm silicon photonics foundry. Optical Engineering. 2025;64(5):057103. https://doi.org/10.1117/1.OE.64.5.057103
5. AIM Photonics. Base Active PIC. The Research Foundation for the State University of New York; c2026 [accessed 2026 Aug 25] https://www.aimphotonics.com/base-active-pic
6. AIM Photonics. Electronic Interposer. The Research Foundation for the State University of New York; c2026 [accessed 2026 Aug 25] https://www.aimphotonics.com/electronic-interposer
7. Chen J et al. High-power-compatible thick silicon-on-insulator waveguide: an implementation in optical phased array. IEEE Photonics Journal. 2026;18(1):1–6. https://doi.org/10.1109/JPHOT.2026.3652317

Appendix. Derivation of Group Delay

This appendix documents the sensitivity of the S-parameter matrix that is used directly to compute group delay. The implementation of this definition into our Jax-based solver removes the need to approximate group delay with finite differences, increasing accuracy of the computation and stability of the method, because the S-matrix computation itself and its derivatives can be obtained directly from the Jax implementation's automatic differentiation.

The wavelength or frequency-dependent phase response of a circuit is used to compute the group delay.

$$\Delta\tau_{group} = -\frac{\delta\phi(\omega)}{\delta\omega} \tag{A-1}$$

or

$$\Delta\tau_{group} = \frac{\delta\phi(\lambda)}{\delta\lambda}[\frac{\lambda^2}{2\pi c}] \tag{A-2}$$

The complex S parameter is given by $S = |S|e^{j\phi}$. This implies

$$ln(S) = ln(|S|e^{j\phi}) \tag{A-3}$$

$$= ln(|S|) + j\phi. \tag{A-4}$$

From the chain rule, we observe that

$$\frac{\delta ln(S)}{\delta\lambda} = \frac{1}{S}\frac{\delta S}{\delta\lambda}. \tag{A-5}$$

Taking the derivative of both sides of Equation A-4 with respect to λ:

$$\frac{1}{S}\frac{\delta S}{\delta\lambda} = \frac{\delta}{\delta\lambda}ln(|S|) + j\frac{\delta\phi}{\delta\lambda}. \tag{A-6}$$

Denoting the complex conjugate with $*$, and the identity $ZZ^* = |Z|^2$, the left-hand side of the equation can be simplified:

$$\frac{S^*}{S^*}\frac{1}{S}\frac{\delta S}{\delta\lambda} = \frac{1}{SS^*}\frac{S^*\delta S}{\delta\lambda} = \frac{1}{|S|^2}\frac{S^*\delta S}{\delta\lambda}. \tag{A-7}$$

Both $\frac{\delta}{\delta\lambda}ln(|S|)$ and $\frac{\delta\phi}{\delta\lambda}$ are purely real quantities. Retaining only the imaginary component of each term,

$$Im[\frac{1}{|S|^2}\frac{S^*\delta S}{\delta\lambda}] = \frac{\delta\phi}{\delta\lambda}. \tag{A-8}$$

Therefore,

$$\frac{\delta\phi}{\delta\lambda} = \frac{1}{|S|^2}Im[\frac{S^*\delta S}{\delta\lambda}]. \tag{A-9}$$

Substituting into our formula for group delay,

$$\Delta\tau_{group} = \frac{\lambda^2}{2\pi c|S|^2}Im[\frac{S^*\delta S}{\delta\lambda}] \tag{A-10}$$

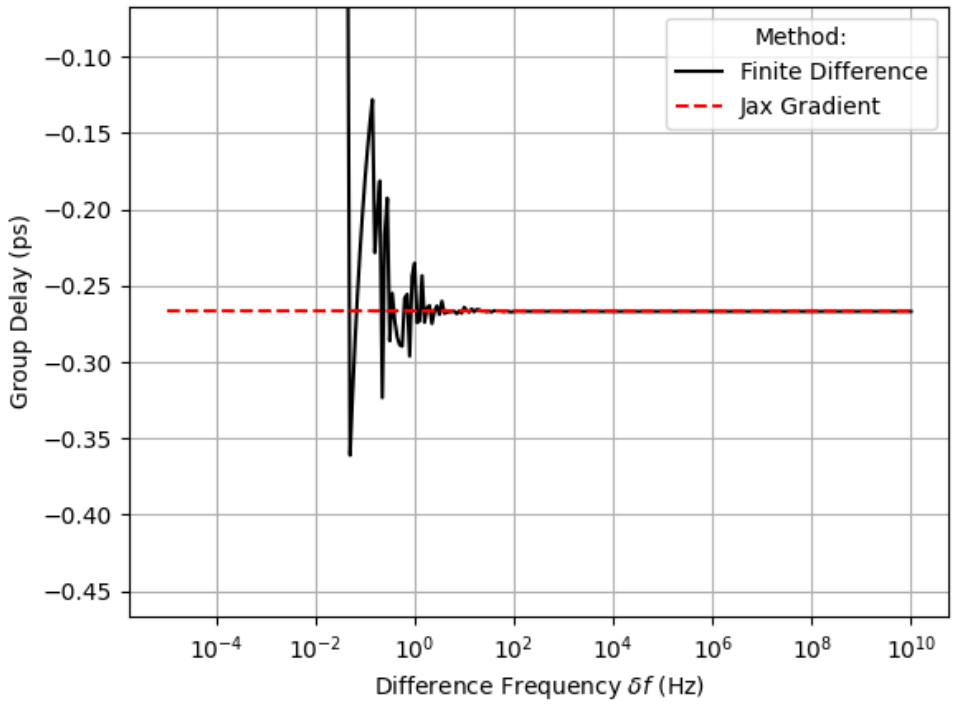


Figure A-1. Jax gradient computation of group delay provides instantaneous computation of group delay at a chosen frequency. The finite difference method can also obtain the group delay accurately but suffers at small offset frequencies due to numerical error.

List of Symbols, Abbreviations, and Acronyms

BGA	Ball-Grid Array
C5ISR	Command, Control, Communications, Computers, Cyber, Intelligence, Surveillance and Reconnaissance
CAD	Computer-Aided Design
CPW	Coplanar Waveguide
DC	Directional Coupler
DEVCOM	U.S. Army Combat Capabilities Development Command
DPDT	Double-Pole, Double-Throw
FDTD	Finite-Difference Time Domain
FSR	Free Spectral Range
FWHM	Full-Width, Half Maximum
LTI	Linear Time-Invariant
MMI	Multi-Mode Interferometer
MPW	Multi-Project Wafer
MZI	Mach-Zehnder Interferometer
OTTD	Optical True Time Delay
OVA	Optical Vector Analyzer
PAA	Phased Array Antenna
PCB	Printed Circuit Board
PDK	Process Design Kit
PIC	Photonic Integrated Circuit
PIF	Prototype Integration Facility
RF	Radio Frequency
SWAP-C	Size, Weight, Power, and Cost
SWIR	Short-Wave Infrared
TAP	Test, Assembly, and Packaging
TEC	Thermo-Electric Cooler
TOS	Thermo-Optic Switch
TSV	Through-Silicon-Via
TTD	True Time Delay
WDM	Wavelength Division Multiplex

Mathematical Symbols

H	Complex-valued transfer function
f	Frequency
ω	Angular frequency ($2\pi f$)
ϕ	Phase
τ	Time delay
$\Delta\tau_{phase}$	Phase delay
$\Delta\tau_{group}$	Group delay
β	Propagation constant
n_{eff}	Effective index of the propagating mode
λ	Wavelength
ΔL	Waveguide length difference
c	Speed of light in vacuum
n_{group}	Group index
L	Path length
L_{FB}	Feedback waveguide length
S_{ij}	S-parameter from port j to port i
Q	Quality factor
K	Coupling constant
$I-V$	Current-Voltage
Ω	Ohm (unit of resistance)

1 (PDF)	DEFENSE TECHNICAL INFORMATION CTR DTIC OCA
1 (PDF)	DEVCOM ARL FCDD RLB CB TECH LIB